Automated Animal Coloration Quantification in Digital Images using Dominant Colors and Skin Classification.

by

Tejas Borkar

A Thesis Presented in Partial Fulfillment
of the Requirements for the Degree
Master of Science

Approved November 2013 by the
Graduate Supervisory Committee:

Lina Karam, Chair
Baoxin Li
Kevin McGraw

ARIZONA STATE UNIVERSITY

December 2013

ABSTRACT

The origin and function of color in animals has been a subject of great interest for taxonomists and ecologists in recent years. Coloration in animals is useful for many important functions like species identification, camouflage and understanding evolutionary relationships. Quantitative measurements of color signal and patch size in mammals, birds and reptiles, to name a few are strong indicators of sexual selection cues and individual health. These measurements provide valuable insights into the impact of environmental conditions on habitat and breeding of mammals, birds and reptiles. Recent advances in the area of digital cameras and sensors have led to a significant increase in the use of digital photography as a means of color quantification in animals. Although a significant amount of research has been conducted on ways to standardize image acquisition conditions and calibrate cameras for use in animal color quantification, almost no work has been done on designing automated methods for animal color quantification.

This thesis presents a novel perceptual-based framework for the automated extraction and quantification of animal coloration from digital images with slowly varying (almost homogenous) background colors. This implemented framework uses a combination of several techniques including color space quantization using a few dominant colors, foreground-background identification, Bayesian classification and mixture Gaussian modelling of conditional densities, edge-enhanced model-based classification and Saturation-Brightness quantization to extract the colored patch. This approach assumes no prior information about the color of either the subject or the background and also the position of the subject in the image. The performance of the proposed method is evaluated for the plumage color of the wild house finches.

Segmentation results obtained using the implemented framework are compared with manually scored results to illustrate the performance of this system. The segmentation results show a high correlation with manually scored images. This novel framework also eliminates common problems in manual scoring of digital images such as low repeatability and inter-observer error.

To my loving parents and brother Varun.

ACKNOWLEDGMENTS

I would like to acknowledge the strong guidance and invaluable support of my thesis advisor Dr. Lina J. Karam in helping me bring this thesis to fruition. I would like to thank Dr. Baoxin Li and Dr. Kevin J. McGraw for agreeing to serve on my committee and providing valuable suggestions. I would also like to thank Dr. Mathieu Giraudeau for his time and support towards this work.

I would like to acknowledge the support provided by all the members of the Image, Video and Usability (IVU) lab. I would specially like to acknowledge the extremely valuable assistance provided by my fellow lab mates Charan Prakash, Vinay Kashyap and Bashar Haddad. I would like to make a special mention of my close friends Shreyas, Pratik, Rohan and Manjiri for their constant support and encouragement throughout my journey. Last but definitely not the least, I would like to express my utmost gratitude to my parents and elder brother Varun for their strong love and support all throughout my journey.

TABLE OF CONTENTS

Page

LIST OF TABLES

Table Page

LIST OF FIGURES

Figure Page

Figure Page

CHAPTER 1

INTRODUCTION

This chapter presents the motivations behind the work in this thesis and briefly summarizes the contributions and organization of the thesis.

1.1 Motivation

The origin and function of coloration in animals has been a topic of immense interest and research for taxonomists and ecologists [1], [2]. Humans have always been intrigued by the bright color patterns observed in various animal species such as the bright plumage colors in most birds or the various multicolor patterns on the wings of butterflies, which is unlike the murky and earthen colors observed in most mammals. This coloration in animals serves many important functions like camouflage, mate selection during breeding, sexual dimorphism and species identification, to name a few [1].

The coloration in animals is a result of a number of different factors. For example, the earth tone, gray, black and brown color observed in most mammals is produced due to a pigment called melanin [3], while the bright plumage coloration observed in birds is the result of a combination of melanin based color, carotenoid pigment based color and structural color due to feathers. Understanding the origin of these color signals and their quantification helps researchers in getting a better understanding of the environmental conditions that affect the habitat and breeding of these animal species. For example, melanin and carotenoid pigments are the most prominent pigments responsible for coloration in birds. Melanin is responsible for the black, gray, brown and earth tone colors present in most birds [3]. Since melanin is produced within the body, melanin based color variation is not strongly correlated to environmental changes [1]. Carotenoid

pigments however, are not produced within the bird's body and are actually acquired through the bird's diet. Carotenoid pigments are responsible for the bright red, orange and yellow plumage colors observed in many birds [4]. Since the carotenoid pigments are derived from diets, quantitative measurements of these bright plumage colors provide great insights into the quality of diet, habitat and individual health of the these birds. Such measurements are also believed to be strong indicators of sexual selection cues [5]. Since environmental conditions and dietary changes affect the carotenoid pigment concentrations in birds, plumage coloration measurement in birds is an important trait for ecologists, taxonomists, conservationists and sustainability scientists. These measurements have been also used for subspecies identification [6].

Animal color quantification refers to the approach of characterizing the coloration observed in individual animals using colorimetric values such as the hue, saturation and brightness in HSB space, the L*, a* and b* values in CIELAB space etc. and using statistical descriptors such as the mean and variance for describing the variation of these values across different specimens of the same species. There are two main methods which are widely used to measure animal color patterns: spectrophotometry and digital photography [7]. But before the advent of spectrometry and digital imaging based approaches, researchers used to measure animal color pattern using color charts [8]-[10]. The observer would record the color of the animal by matching it to the closest color on a chart consisting of different colors. The closest value of color chosen on the color chart was based purely on the color perception of the human observer. This method resulted in low intra and inter-observer repeatability and was unable to measure colors outside the visible spectrum of humans [7]. This approach was widely used due to its ease of use,

before digital cameras and spectrometers became more affordable. Spectrometry based approaches measure color signal information using the reflectance spectra [11]. A spectrometer is used to measure the intensity of light reflected over a range of wavelengths. A major advantage of spectrometry is that it can be used to measure color signals that lie outside the visible spectrum and as such cannot be measured by methods that rely on human visual perception [7]. Photography has been used for animal coloration studies for a long time now, but recent advances in digital cameras and sensors have led to a significant increase in the use of digital photography as a means of color quantification in animals [1], [2]. Digital photography based approaches provide great benefits over traditional spectrometry, like faster data acquisition rates, ease of use and minimal equipment requirements [2], [7]. Also image based approaches can employ customized programs for simultaneously computing multiple parameters like patch size and colorimetric values from the same image [2].

A lot of the work in the field of digital photography based animal color quantification has been focused on developing methods for measuring animal coloration by standardizing illumination conditions [2], linearizing sensor response curves [12] and camera calibration [13]. However, virtually no work has been done on developing an efficient automated method for extracting animal coloration values and patch sizes from digital images. Most current studies that involve color quantification employ time consuming manual processing of images [14]-[16]. This involves drawing a region enclosing the color patch on the animal using image editing software and analyzing the color values at all pixels in the outlined region by comparing them to a reference color control patch in the same image. Such a method may be prone to problems such as low

repeatability of results, inter-observer error and reduced accuracy across time (observer fatigue) over large datasets. As a result, there is a need for an automated framework that provides fast, repeatable and efficient extraction of animal coloration values in digital images.

Out of the many bright colored animal species studied as a part of animal color quantification, the house finch (*Haemorhous mexicanus)* is an important one and has been widely studied [17]-[19]. The house finches can have widely varying plumage colors from bright red to orange–yellow. As stated earlier, these bright colors like red and yellow are the result of carotenoid based pigments which are derived from the bird's diet [4]. Color measurements for the house finch can help researchers understand mating success [20], [21] and the impact of environment on the quality of diet [1]. Fast moving animal species such as the house finch need to be restrained by human hands during image acquisition. The plumage color of the house finch is also very similar, at times, to the color of the human hands holding the bird in place and this makes it much more challenging to segment the plumage color of these birds. For these reasons, the house finch is used as the main test subject in this study and its bright plumage color is used for evaluating the performance of the proposed system.

1.2 Contributions

In this thesis, a novel perceptual-based approach for the automated extraction of animal coloration variables such as hue, saturation, brightness, and patch size, from digital images with slowly varying background colors, is presented. In this proposed framework, the input image is first coarsely segmented into few classes using dominant colors. The dominant colors are identified by detecting the local peaks in the image color distribution

computed in a perceptually uniform color space. The required foreground class is then identified by eliminating the most dominant color in the color histogram of the image as the color of the background region. In the case of fast moving animals, the animal specimen is held in position by human hands. Therefore, to account for this latter case, the foreground region is further segmented into skin and non-skin regions to identify the region of human hands in the image. The skin/ non-skin classification is performed using a Bayesian skin color classifier, with the required skin conditional density modelled as a Gaussian mixture model. This is followed by an edge-enhanced model-based classification scheme to eliminate the outlier skin regions. Finally, a novel perceptual-based Saturation-Brightness quantization is implemented for the removal of perceptually insignificant colors and only retaining the colors of interest (bright colors). The perceptual based Saturation-Brightness quantization helps to refine the region of interest by eliminating perceptually insignificant colors, such as black, gray and white while preserving the perceptually visible (bright) colors. This perceptual-based quantization step is useful for quantifying carotenoid pigment based colors and can be avoided if only colors such as black, gray and white need to be quantified.

1.3 Thesis Organization

The organization of this thesis is as follows: Chapter 2 provides the background for the different color spaces used for quantization, and basic concepts related to Bayes classifier and Gaussian mixture models used for modelling conditional densities. Chapter 3 describes the current manual, semi-automated and automated methods that are related to this thesis. Chapter 4 describes the proposed animal color extraction and quantification framework. Chapter 5 presents performance results for a set of images, and a comparison

between the results produced by the proposed automated framework and manual scoring methods. Chapter 6 summarizes the contributions of this thesis and proposes future directions of research.

CHAPTER 2

BACKGROUND

This chapter provides some background information about the different color spaces used in this thesis, Bayes classifier and Gaussian mixture modelling of multimodal distributions, all of which is useful in understanding the implemented framework. Section 2.1 describes the different color spaces used in this framework. Section 2.2 explains the expectation-maximization approach for deriving Gaussian mixture models. Section 2.3 describes Bayesian decision theory for classification.

2.1 Color Spaces

A color space is a multi-dimensional space representation that describes every color produced by a color model as a unique tuple of three or four numbers called color components. It is basically a combination of a color model that describes how various observed colors can be produced and an associated mapping function that maps every color to a unique point in a multi-dimensional space. The co-ordinates of such a point represent the relative amounts of the individual color components of the considered color model, which combine to produce the observed color. Usually, most color spaces use a three-element tuple representation for colors and the 3 axes of the color space represent the three fundamental color components of the color model used. Since a color space is just a combination of a color model and a mapping function, many different combinations of color models and mapping functions can be used to represent the same observed color.

In recent years, many different color space representations have been introduced and the choice of a particular color space usually depends on the application. The various color spaces are mainly divided into the following groups [22]:

a) Primary spaces

   The primary spaces are based on the idea that every color can be produced by mixing appropriate amounts of three primary colors.

b) Luminance-chrominance spaces

   The luminance-chrominance spaces refer to color spaces in which one of the three color space components represents luminance information and the other two represent chrominance information.

c) Perceptual spaces

   Perceptual spaces are designed to make color spaces more intuitive to humans. In these color spaces, a color is represented by its hue, saturation and intensity, just as a human would describe the same color.

d) Independent axis spaces

   Independent axis color spaces are derived by using different statistical approaches to minimize the correlation between the individual components of the color space.

In this section, we discuss the three different color spaces which are used in the implemented framework. The three color spaces used are the CIE (*R, G, B*), the CIE (*L*, a*, b**) and the HSV color spaces.

2.1.1 CIE (R, G, B) color space

The CIE (*R, G, B*) color space is a primary color space based on the trichromatic theory, which assumes that every color can be expressed as a combination of appropriate

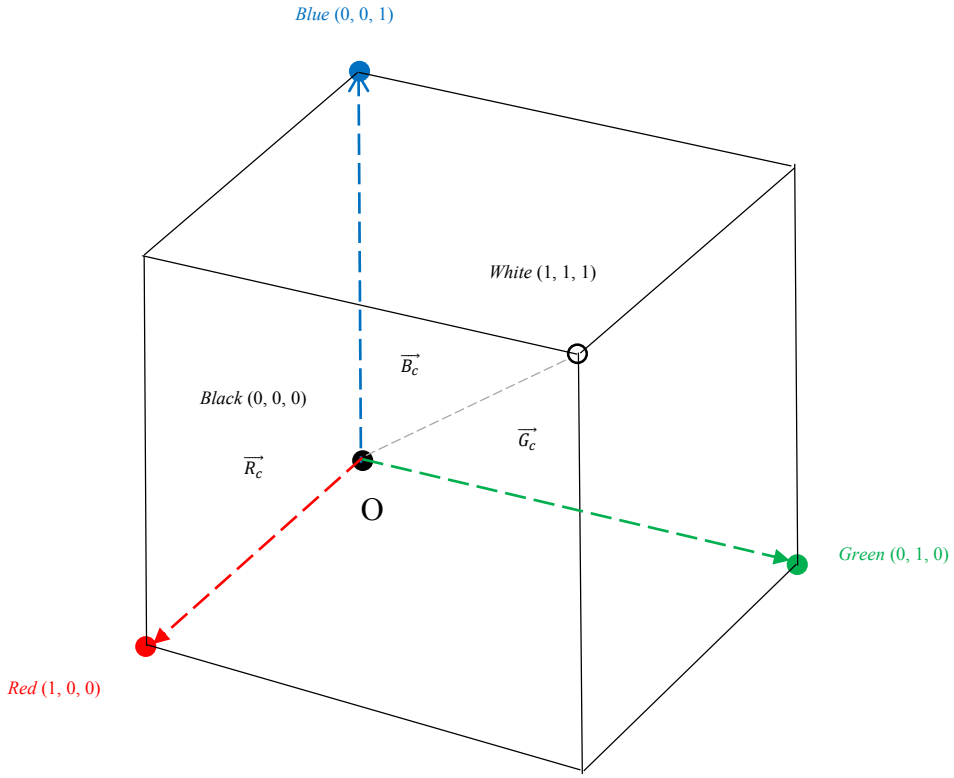

Fig. 1 *RGB* color cube.

amounts of three primary colors. Analogous to the human eye, the three primary components of the CIE (*R, G, B*) are red, blue and green. The color space is derived from color matching experiments that were conducted using the three color primaries denoted by R_c, G_c and B_c, which are monochromatic color signals of wavelengths 700.0 nm, 546.1 nm and 435.8 nm, respectively [22]. It is possible to obtain many different (*R, G, B*) color spaces depending on the choice of wavelengths for the primaries. However, the CIE (*R, G, B*) color space is considered as a reference (*R, G, B*) color space as it defines the *standard observer,* whose eye spectral response represents the average eye spectral response of a human observer [22]. Fig. 1 illustrates the *RGB* color cube which defines the (*R, G, B*) color space and the three normalized vectors $\overrightarrow{R_c}$, $\overrightarrow{G_c}$ and $\overrightarrow{B_c}$, which represent

the three primaries (*R, G, B*). The normalized vectors $\overrightarrow{R_c}$, $\overrightarrow{G_c}$ and $\overrightarrow{B_c}$ form the principal axes of the 3D vector space and intersect at the origin of the color space denoted by point O. Every color is represented by a point C in the color cube and defined by a vector $\overrightarrow{OC}$ with the projections of $\overrightarrow{OC}$ on the primary axes representing the tristimulus values R_c, G_c and B_c , which correspond to the relative amounts of the red, green, and blue primaries, respectively, that combine to form the considered color. The tristimulus values for a particular set of primaries are defined by color mapping functions, also known as color matching functions. The normalized color matching functions for the CIE (*R, G, B*) color space are denoted by $\bar{r}(\lambda)$, $\bar{g}(\lambda)$ and $\bar{b}(\lambda)$. For a known set of color matching functions, the normalized tristimulus (R_c, G_c, B_c) values for a color with power spectral distribution *I(λ)* are given by [23]:

$$\boldsymbol{R_c} = \int_0^\infty I(\lambda)\, \bar{r}(\lambda) d\lambda \tag{1}$$

$$\boldsymbol{G_c} = \int_0^\infty I(\lambda)\, \bar{g}(\lambda) d\lambda \tag{2}$$

$$\boldsymbol{B_c} = \int_0^\infty I(\lambda)\, \bar{b}(\lambda) d\lambda \tag{3}$$

The origin O with normalized tristimulus values (0, 0, 0) represents the color black and the color white is defined by the normalized tristimulus values (1, 1, 1). The dotted gray colored line in Fig.1 is known as the gray axis or the neutral color axis [22]. For every point on this line, the *x, y,* and *z* co-ordinates are equal and as a result each point on this line represents a different shade of gray between black and white. The primary colors red, green and blue are given by (1, 0, 0), (0, 1, 0) and (0, 0, 1), respectively.

2.1.2 CIE (L, a*, b*) color space (also known as CIELAB)*

The (*R, G, B*) color space has a few drawbacks including the following:

a) The tristimulus values are dependent on the luminance, which is a linear combination of the tristimulus values.

b) The (*R, G, B*) color spaces are device dependent and it is possible to formulate many different (*R, G, B*) color spaces with different primaries and color matching functions.

c) The (*R, G, B*) color spaces are not perceptually uniform.

Perceptual uniformity means that equal changes in color values should correspond to an equal color difference perceived by a human.

To overcome the problem of perceptual non-uniformity and device dependence, the CIE formulated an alternate perceptually uniform color space known as (*L**, *a*, b**) or CIELAB. The (*L**, *a*, b**) color space is a luminance-chrominance space, where unlike the (*R, G, B*) color space, the luminance (brightness) component is completely separated from the chrominance (color) component of the input visual signal. The *L** component represents the brightness response of the human eye to a visual stimulus, while the *a** and *b** components represent the green-red color opposition and blue-yellow color opposition, respectively [22]. The forward transform that converts values in CIE (*R,G,B*) color space to corresponding values in CIELAB color space is given by [24],

$$\begin{bmatrix} X \\ Y \\ Z \end{bmatrix} = \begin{bmatrix} 0.49018 & 0.30987 & 0.19993 \\ 0.17701 & 0.81232 & 0.01066 \\ 0 & 0.01007 & 0.98992 \end{bmatrix} \begin{bmatrix} R_c \\ G_c \\ B_c \end{bmatrix} \tag{4}$$

$$L^* = 116 * f\left(\frac{Y}{Y_n}\right) - 16 \tag{5}$$

$$a^* = 500 * \left[f\left(\frac{X}{X_n}\right) - f\left(\frac{Y}{Y_n}\right) \right] \tag{6}$$

$$b^* = 200 * \left[f\left(\frac{Y}{Y_n}\right) - f\left(\frac{Z}{Z_n}\right) \right] \tag{7}$$

$$f(t) = \begin{cases} t^{\frac{1}{3}}, & t > \left(\frac{6}{29}\right)^3 \\ \frac{1}{3}\left(\frac{29}{6}\right)^2 t + \frac{4}{29}, & otherwise. \end{cases} \tag{8}$$

where (R_c, G_c, B_c) represents the normalized tristimulus values in CIE (R, G, B) color space, (X, Y, Z) represents tristimulus values in CIEXYZ color space, (X_n, Y_n, Z_n) represents tristimulus values of the reference white point in CIEXYZ color space and (L^*, a^*, b^*) represents the corresponding tristimulus values in CIELAB color space. Similarly, the backward transform that converts values from CIELAB to CIE (R, G, B) color space is given by,

$$Y = Y_n * f^{-1}\left(\frac{1}{116}(L^* + 16)\right) \tag{9}$$

$$X = X_n * f^{-1}\left(\frac{1}{116}(L^* + 16) + \frac{1}{500}a^*\right) \tag{10}$$

$$Z = Z_n * f^{-1}\left(\frac{1}{116}(L^* + 16) - \frac{1}{200}b^*\right) \tag{11}$$

$$f^{-1}(t) = \begin{cases} t^3, & t > \left(\frac{6}{29}\right) \\ 3\left(\frac{6}{29}\right)^2 \left(t - \frac{4}{29}\right), & otherwise. \end{cases} \tag{12}$$

$$\begin{bmatrix} R_c \\ G_c \\ B_c \end{bmatrix} = \begin{bmatrix} 2.36353 & -0.89582 & -0.46771 \\ -0.51511 & 1.42643 & 0.08867 \\ 0.00524 & -0.01452 & 1.00927 \end{bmatrix} \begin{bmatrix} \mathrm{X} \\ \mathrm{Y} \\ \mathrm{Z} \end{bmatrix} \tag{13}$$

2.1.3 (H, S, V) color space

Although the CIELAB color space is perceptually uniform, it is not very intuitive and perceptually relevant for day-to-day applications of color systems such as graphics and

fine art. Even the (*R, G, B)* color space is not intuitive for the above mentioned applications as the chrominance and luminance components in the (*R, G, B)* color space are not separate and the Cartesian co-ordinate system for representing colors is not perceptually relevant. To make the idea of color and brightness more intuitive, perceptually relevant and useful for general applications, the (*H, S, V*) color space was designed by R. Smith [25] and represents a color in terms of its *hue* (H), *saturation* (S), and *value* (V). The *hue* of a color represents a component of the visual stimulus that helps us perceive a patch of color to be similar to one of the known colors like red, blue, green, yellow or a combination of the two. The extent to which a pure color must be diluted with white to resemble a shade of perceived color can be represented by the term *dilution*. The saturation component is inversely proportional to the dilution. A high saturation value represents less dilution with white and vice versa. The highest *saturation* value represents a pure color without any dilution with white. The lowest *saturation* value represents the color white (maximum dilution). The value component measures how light or dark a particular color is in the image [25]. The (*H, S, V*) color space is a cylindrical representation of the *RGB* color cube as shown in Fig. 2.

The (*H, S, V*) color space model shown in Fig. 2 can be derived by tilting the RGB cube and resting it on one of its corner, such that the color black is at the origin and the white is directly above it along the vertical axis as shown in Fig. 3. The projection of this cube results in a hexagonal plane with the pure primary and secondary colors located at the vertices as shown in Fig. 3. The neutral axis or the gray line of the RGB cube is mapped into the origin in the projection and the final cylindrical *(H, S, V*) representation is obtained by extending the hexagonal plane along the vertical axis and warping the

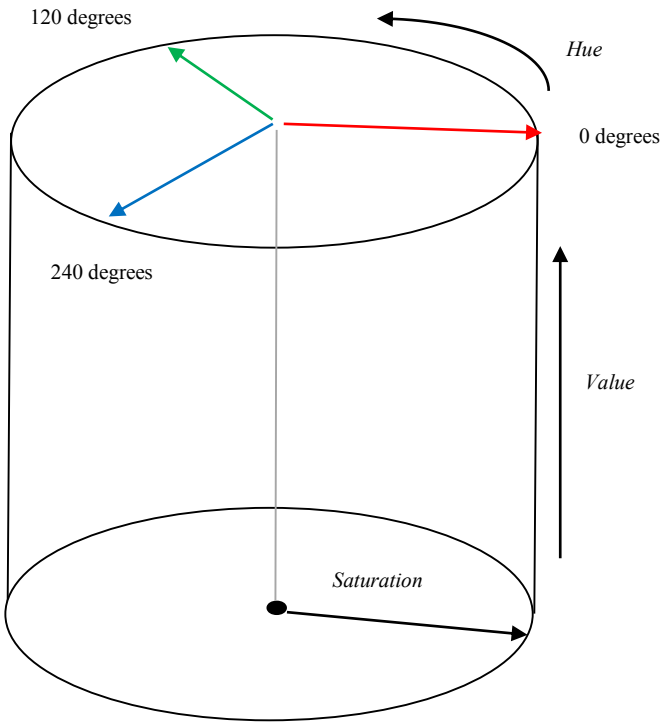

Fig. 2 *HSV* model representation using cylindrical co-ordinates.

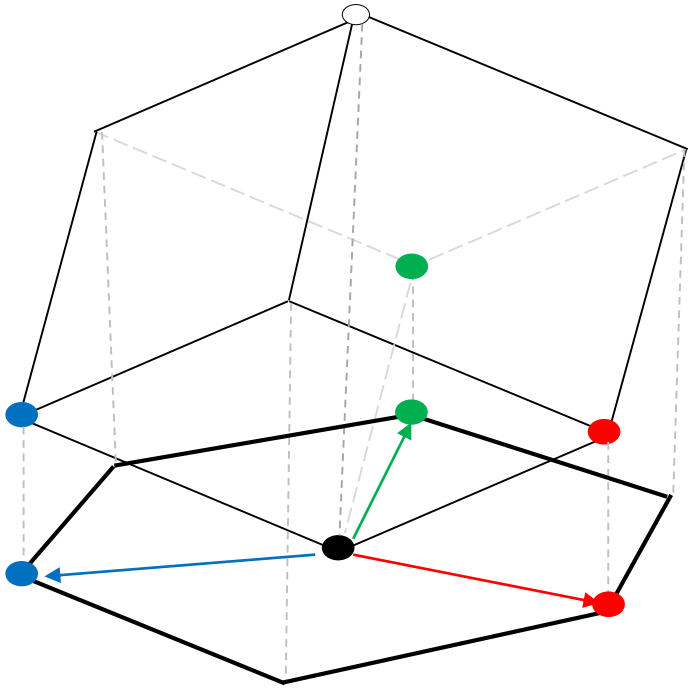

Fig. 3 Projection of tilted *RGB* cube on a plane.

hexagon into a circle. The *hue* is the angle of the vector formed by the projection of a point in the RGB cube onto the hexagonal plane, measured about the vertical axis with red at 0°, green at 120° and blue at 240°. The saturation is measured along the radius of the cylinder over a range of [0, 1] as shown in Fig. 2. The value component forms the vertical axis of the cylindrical representation, with a range of values between [0, 1]. All points that lie on the vertical axis have a *saturation* component equal to zero and as a result have no color information associated with them. These points represent the different shades of gray between black and white and have no specific value of *hue* defined for them. As these points have no unique *hue* value defined for them, it is possible to identify and represent shades of gray including black and white in this color space by just computing the *saturation* and *value* components, independent of the *hue* component. Black can be represented by the point $\{S=0,\ V=0\}$, while white is represented by $\{S=0,\ V=1\}$ and shades of gray are represented by points $\{S = 0, 0 \leq V \leq 1\}$ on the vertical axis. The transformation of normalized tristimulus (R_c, G_c, B_c) values to (H, S, V) values is given by [25]:

$$C = \max(R_c, G_c, B_c) - \min(R_c, G_c, B_c) \tag{14}$$

$$H = \begin{cases} 60^{\circ} * \left(\frac{G_c - B_c}{C} \bmod(6)\right), & \text{if } \max(R_c, G_c, B_c) = R_c \\ 60^{\circ} * \left(\frac{B_c - R_c}{C} + 2\right), & \text{if } \max(R_c, G_c, B_c) = G_c \\ 60^{\circ} * \left(\frac{R_c - G_c}{C} + 4\right), & \text{if } \max(R_c, G_c, B_c) = B_c \\ undefined & C = 0 \end{cases} \tag{15}$$

$$S = \begin{cases} 0, & C = 0 \\ \frac{C}{\max(R_c, G_c, B_c)}, & \text{otherwise.} \end{cases} \tag{16}$$

$$V = \max(R_c, G_c, B_c) \tag{17}$$

$$xmod(y) = x - \left\lfloor \frac{x}{y} \right\rfloor * y \tag{18}$$

where $\left\lfloor \frac{x}{y} \right\rfloor$ represents a flooring operation in which the quotient of $\frac{x}{y}$ is rounded downwards.

2.2 Gaussian Mixture Model Estimation using Expectation-Maximization

In most classification problems, the conditional probability densities cannot be accurately represented as unimodal distributions and usually take the shape of complex multi-modal distributions. A Gaussian Mixture Model (GMM) is a parametric probability distribution function that is widely used for modelling such complex shaped multi-modal distributions. The GMM is a weighted sum of multiple unimodal component Gaussian densities given by the equation,

$$p(x) = \sum_{i=1}^{m} w_i \; g(x|\mu_i, \Sigma_i) \tag{19}$$

where x is an N-dimensional vector, w_i is the mixture weight and $g(x|\mu_i, \Sigma_i)$ is the component density for the i^{th} Gaussian component. The component density is given by,

$$g(x|\mu_i, \Sigma_i) = \frac{1}{(2\pi)^{N/2}|\Sigma_i|^{1/2}} \exp\left\{-\frac{1}{2}(x-\mu_i)^T \Sigma_i^{-1}(x-\mu_i)\right\} \tag{20}$$

where μ_i and Σ_i represent, respectively, the mean vector and covariance matrix of the i^{th} component density. The mixture weights also satisfy the following constraint:

$$\sum_{i=1}^{m} w_i = 1 \tag{21}$$

Due to the parametric nature of the model, the entire model can be accurately represented using just the mean vector μ_i, covariance matrix Σ_i and mixture weight w_i for each component Gaussian density and these parameters can be estimated from a training data set using a maximum-likelihood approach.

The GMM parameters are estimated iteratively, using a special case of the Expectation-Maximization algorithm [26]. Given an initial estimate of the GMM model, the E-M algorithm iteratively estimates a model λ, such that $p(X|\lambda_{t+1}) \geq p(X|\lambda_t)$ at iteration *t+1* for a given training set X=$\{x_1, x_2, \ldots, x_{T_1}\}$ with T_1 training samples. λ represents the set of component parameters $\{w_i, \mu_i, \Sigma_i\}$ for the M component densities. The likelihood $p(X|\lambda_{t+1})$, posterior probability, mean vector, covariance matrix and mixture weight is recomputed for all components at every iteration till a stopping criteria that maximizes the likelihood function is reached. At every iteration, the posterior probability for each component and training sample is first calculated as:

$$P_{i,j}^{(t)} = \frac{w_i^{(t)} g(x_j|\mu_i^{(t)}, \Sigma_i^{(t)})}{\sum_{k=1}^{m} w_k^{(t)} g(x_j|\mu_k^{(t)}, \Sigma_k^{(t)})} \tag{22}$$

where *t* represents the iteration number, *i* represents the component number and x_j is the j^{th} training sample in X. Next, the updated mean vector, covariance matrix and mixture weight for the i^{th} component are calculated as:

$$w_i^{(t+1)} = \frac{1}{T_1} \sum_{j=1}^{T_1} P_{i,j}^{(t)} \tag{23}$$

$$\mu_i^{(t+1)} = \frac{\sum_{j=1}^{T_1} P_{i,j}^{(t)} x_j}{\sum_{j=1}^{T_1} P_{i,j}^{(t)}} \tag{24}$$

$$\Sigma_i^{(t+1)} = \frac{\sum_{j=1}^{T_1} P_{i,j}^{(t)} (x_j - \mu_i^{(t+1)})(x_j - \mu_i^{(t+1)})^T}{\sum_{j=1}^{T_1} P_{i,j}^{(t)}} \tag{25}$$

$$L(x; \lambda_{t+1}) = \prod_{j=1}^{T_1} p(x_j|\lambda_{t+1}) \tag{26}$$

where λ_{t+1} represents the model for iteration t+1 and $L(x; \lambda_{t+1})$ represents the likelihood function at iteration t+1. The E-M algorithm is terminated when the difference between $\ln L(x; \lambda_{t+1})$ and $\ln L(x; \lambda_t)$is lesser than a pre-decided threshold.

2.3 Bayesian Decision Theory

Bayesian decision theory is an important statistical approach used in many pattern classification tasks. The approach uses a probability distribution to evaluate the merit of various classification decisions along with the cost associated with making each classification decision. This approach assumes that a particular classification task can be formulated as a problem based on probability and, given all the relevant conditional densities and prior probabilities, predicts the best classification rule as the one that minimizes the probability of error [27].

For an object classification task, a classification can be performed by assigning the observed object to the class w_i with the highest a priori probability $P(w_i)$. However, a measured value or feature x that represents an attribute of the object can be used to make a more robust decision that minimizes the probability of error. The measured value x can be a single value or a vector of values representing a feature. Consider a general classification problem where we have a measurement value x which is continuous and the classification scheme has to identify the class w_i, i = 1, 2, 3,…..,M, that produced the measurement x. The a priori probabilities represented by $P(w_i)$, i = 1, 2, 3,….., M, and the likelihood functions or class conditional densities represented as $p(x|w_i)$, i = 1, 2, 3,….., M, are assumed to be completely known. The probability of error associated with the object being assigned to class w_j, given a measurement x is given as:

$$P(error|x) = \sum_{i=1, i\neq j}^{M} P(w_i\,|x). \tag{27}$$

This can be re-written in another form as,

$$P(error|x) = 1 - P(w_j|x) \tag{28}$$

due to the relation, $\sum_{i=1}^{M} P(w_i|x) = 1$. The average probability of error is given by:

$$P(error) = \int_{-\infty}^{\infty} P(error|x)p(x)dx \tag{29}$$

where $p(x)$ can be expressed as follows:

$$p(x) = \sum_{i=1}^{M} p(x|w_i)P(w_i). \tag{30}$$

As per Bayes' decision theory, the best decision chooses the class that minimizes (27). From (28), we observe that $P(error|x)$ is minimized when $P(w_{j|}|x)$ is maximized. Thus the best decision chooses the class w_j for which $P(w_j|x)$ is maximum. Using Bayes' theorem, we can write $P(w_j|x)$ as,

$$P(w_j|x) = \frac{p(x|w_j)P(w_j)}{p(x)}. \tag{31}$$

Since $p(x)$ is just a scaling factor and is the same for all classes, we can ignore $p(x)$ to get the final form of the Bayes' decision theory. For an *M* class classifier, given a measurement *x*, the Bayes classifier chooses the class w_j such that:

$$p(x|w_j)P(w_j) \geq p(x|w_i)P(w_i) \qquad \forall i \neq j. \tag{32}$$

The expression in (28) can be further simplified for a binary classifier with equal prior probabilities for both classes. In this latter case, for a given measurement x, we decide to choose class w_1 if

$$p(x|w_1) \geq p(x|w_2) \tag{33}$$

and class w_2 otherwise.

CHAPTER 3

RELATED WORK

This chapter summarizes the previous work related to animal coloration quantification methods using digital photography. Section 3.1 describes few popular manual software methods. Section 3.2 describes an automated approach for intensity quantification of animal patterns in gray scale images.

Digital image processing and computer vision approaches have been widely used for many automated image and video analysis applications such as biometrics, biomedical imaging, microscopy, surveillance etc. For example, automated image processing methods have been implemented for face, fingerprint recognition and matching [28], cell migration in microscopy images [29], identifying and tracking people and objects in videos for surveillance, computer aided lesion detection and diagnosis in mammography [28] etc. The range of applications for automated image analysis is ever expanding.

There has been a steady increase in the use of digital photography for quantifying animal and plant color patterns in recent years [2], [30], [31], due to the fast data acquisition speeds and permanent storage capability provided by it [2]. The use of digital photography in coloration studies also allows for multi-parameter measurements and enables researches to obtain measurements in the wild without the trouble of managing expensive and bulky equipment. Although digital photography provides several useful benefits over traditional animal coloration quantification approaches like spectrometry [7], [2], it does have a few important limitations that affect the accurate measurement and quantification of coloration in animals. Digital camera sensors have non-linear intensity

response curves and the colors reproduced in images are device-dependent due to the variation in spectral responses of different camera sensors [2]. As a result, if not corrected for these effects, the same image acquired using different digital cameras would provide different color quantification results. Also, a lot of the recent digital cameras employ built in image pre-processing and compression algorithms that modify the initial raw intensity data recorded by the camera.

In order to better leverage the benefits of digital photography, work has been done on developing methods for measuring animal coloration by standardizing illumination conditions [2], linearizing sensor response curves [12] and camera calibration [13]. However, the idea of implementing an efficient and robust automated software framework for quantifying animal coloration has largely been unexplored [2].

3.1 Manual Software Methods

The most popular and widely used current manual method involves the use of a digital photo editing software like Adobe Photoshop [32], GIMP [33], ImageJ [34] etc. with user-driven inputs to identify the region of interest (henceforth referred to as ROI) and quantify it [35]. The ROI is identified by using a magic wand tool that takes user-provided locations for identifying the ROI. After an initial start location is provided in the image by the user, the software implements a region growing method to merge regions around the user-provided start location, based on the similarity of color. The sensitivity of the region merging process to color differences is controlled by a threshold and the ROI is refined by repeated readjustments of this threshold by the user. The color quantification is achieved using histogram based tools or external plugins provided for measuring image intensities in these software packages. The method illustrated in [35] can be considered as

a semi-automated method as opposed to the prior manual methods of actually drawing a contour tightly enclosing the ROI using a freehand region drawing tool [14]-[16]. Identifying the ROI by drawing a closed contour around it using a freehand drawing tool in an image editing software is an extremely cumbersome task, may provide low repeatability of results and the accuracy of results is largely user dependent. The semi-automated user-driven method in [35] explained earlier, uses a user driven region merging process and is more robust and accurate as compared to the manual method of selecting the region of interest using a freehand drawing tool. However, the software based semi-automated method also has many limitations. The semi-automated user-driven method can be extremely time consuming, does not provide batch processing capabilities and can result in low intra-photo repeatability. Also, since the region growing process is user controlled, the accuracy of results may be significantly reduced over large datasets, due to user fatigue.

Vortman et al. [36] developed a couple of user-driven MATLAB based software packages called “Hirundo” and “Hirundo feather” for measuring animal coloration and feather coloration. Unlike the user-driven region growing/merging method used in [35], the “Hirundo” tool is based on the idea of two-class quantization of the user selected region to measure the color values of interest. In this method, the user selects a rectangular region enclosing the ROI and the software tool then performs a two-class quantization of the selected region into foreground (ROI) and background. The authors in [36] claim to use a Lloyd-Max quantizer based algorithm for this quantization and a user-defined threshold for adjusting the image region considered to be foreground. However, the authors in [36] do not provide any further details about their quantization scheme.

Given that the Lloyd-Max quantizer is used for generating optimal partitions of continuous geometric regions and the quantization scheme results in [36] can be adjusted using user-defined thresholds, it is unlikely that the Lloyd – Max quantization is being used in the approach in [36]. It is more likely that the quantization of the user-selected region in [36] is performed using just a user-defined threshold, to get the desired ROI. Although using the "Hirundo" tool is not as cumbersome as the method in [35], it suffers from the same limitations as [35]. The requirement of a user-defined region for quantization makes this approach both time consuming and susceptible to inter-observer errors. Also, if the ROI consists of more than one quantifiable color (e.g., Butterfly wing patterns), the two-class quantization process is unable to quantify them separately and the resultant chrominance values of the ROI would correspond to an average of the chrominance values of the quantifiable colors. Such an average value would represent a totally different color than the one to be quantified. For example, if the identified ROI consisted of red and green colored regions, then the tool would most likely provide a quantified chrominance value corresponding to the color yellow. These limitations necessitate the development of an automated framework that is able to automatically characterize multiple colors in the scene in a fast manner, with a high-degree of accuracy and avoid human and inter-observer errors.

3.2 Automated Quantification Method

As mentioned before, most of the research in using digital photography methods for quantifying animal coloration have focused on optimizing the conditions for acquiring images, linearizing camera sensor responses and camera calibration. Virtually no work has been done on implementing a flexible framework for automatically segmenting and

quantifying the different animal coloration patterns in digital images. A couple of approaches for segmenting simple animal coloration patterns in grayscale images, using basic image processing methods such as intensity based thresholding and edge based thresholding were proposed in [2]. In the first approach, the ROI is segmented by converting the 8-bit grayscale image into a binary image using a user-defined threshold, where every pixel belonging to the ROI is assigned a value of 1 and all other pixels are assigned a value of 0. The required threshold value is decided based on prior knowledge of the area to be segmented or some explicit assumption. The second approach uses strong edges to identify the region of interest. This approach is based on the assumption that the boundary of the ROI corresponds to the sharp changes in intensity in an image. These sharp changes in intensity can be identified by detecting the strong edges in the image. Both of these approaches assume some prior knowledge of the data for computing the threshold values and are not designed to segment complex region boundaries found in many animal coloration studies. In contrast, the proposed framework in this thesis assumes no prior knowledge of the location or color of the specimen used for color quantification.

CHAPTER 4

IMPLEMENTED AUTOMATED COLOR QUANTIFICATION SYSTEM

This chapter describes the proposed framework for automated animal coloration extraction and quantification in digital images. The developed framework consists of 4 major steps: extracting the foreground region and excluding the background region using dominant colors, skin/non-skin region classification using a binary Bayesian classifier, removal of outlier skin pixels using an edge-enhanced model, and perceptual-based Saturation-Brightness quantization to refine the region of interest by eliminating perceptually insignificant colors, such as black, gray and white, while preserving the perceptually visible (bright plumage) colors. Section 4.1 presents an overview of the implemented automated animal coloration quantification system. The four major components of the proposed animal coloration quantification framework are described in Sections 4.2 to 4.5. Section 4.6 describes the MATLAB-based software implementation and summarizes the major steps of the proposed algorithm.

4.1 Overview of the Proposed System

In this work, the problem of extracting the animal coloration patches is treated as a color segmentation problem and the proposed approach draws inspiration from the class of image segmentation methods that use a few representative dominant colors for segmenting an image into regions of perceptually homogenous colors.

In many images used for animal color quantification, a standard color strip is placed alongside the bird or animal as shown in Fig. 4. The strip can be used for illumination correction in post-acquisition analysis. In this work, the color strip is

Fig. 4. Original image with the color strip present.

Fig. 5. Binary image showing the detected color square in white, for color strip removal.

Fig. 6. Image obtained after removing the color strip from the image.

detected by searching for the presence of a specific color present in the color strip, using a MMSE (minimum mean squared error) metric. Once the color strip is detected, its color(s) can be quantified and stored for use in color normalization to achieve an illumination-invariant color quantification. Since the color strip is outside the Region-of-Interest (ROI) containing the animal, a cropped image containing the ROI is formed by removing the region containing the detected color strip. Fig. 4 shows the image before color strip removal. The binary mask showing the detected color square in white, used for color strip removal, is shown in Fig. 5. The image after color strip removal is shown in Fig. 6. After color strip removal, the cropped image is processed by the proposed automated animal coloration quantification algorithm (see more below) to extract and quantify the colors in the ROI. In the remainder of this thesis, the term input image refers to the image after color strip removal. Fig. 7 illustrates the block diagram of the proposed algorithm. After color strip removal, a coarse two-class color quantization is performed on the input image in order to segment the image into a background (insignificant region) and a foreground (region containing the object of interest) region.

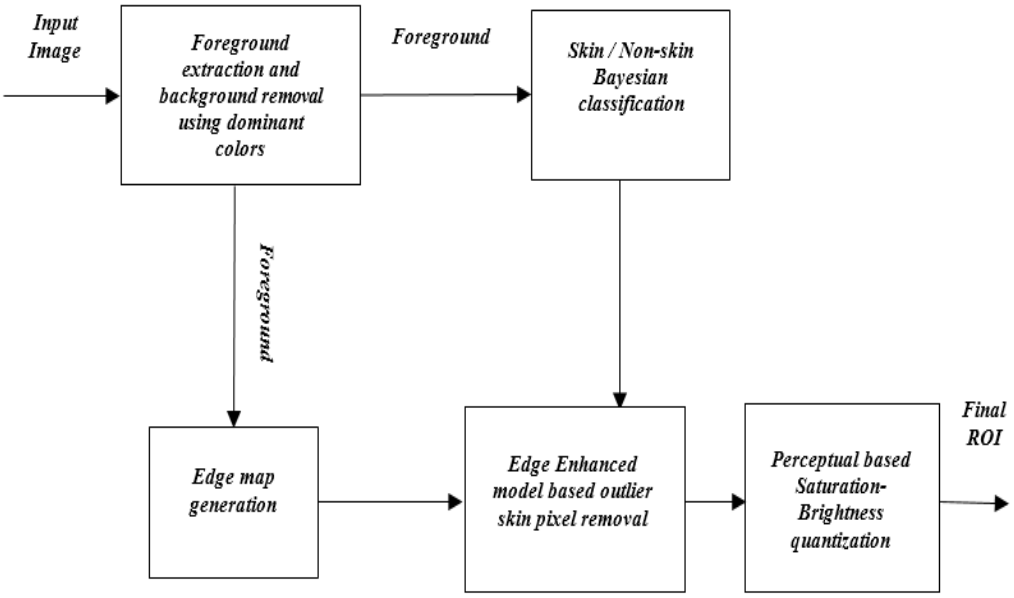

Fig. 7 Block diagram of the proposed framework.

The extracted foreground region is then further processed in order to extract colors corresponding to the bird plumage area, while removing other outlier colors such as colors due to the presence of human hands with or without gloves. If gloves are used, removing the outlier colors is a relatively easy task since the color of the gloves is typically chosen to be significantly different than the colors of interest in the animal. The gloves can be removed using a coarse color quantization scheme similar to the one used in the aforementioned foreground extraction step. If no gloves are used, the problem becomes more challenging since the human skin color can be in many cases similar to the colors of interest in the animal. In order to eliminate the regions corresponding to the human skin colors while preserving the bright animal colors, we propose a novel model-based approach combined with a Bayesian classifier. After regions corresponding to

human skin are removed, the remaining foreground region is subjected to a perceptual-based saturation-brightness quantization that preserves the perceptually visible colors (bright colors like red, yellow, orange etc.) while removing the perceptually insignificant ones. The resulting ROI colors are quantified in terms of their mean hue, saturation and brightness values for each segmented color patch in the ROI. The size of each ROI color patch is also provided as an output by the proposed algorithm. Further details about the foreground extraction and background removal, skin/non-skin classification, edge-enhanced model-based outlier skin pixel removal and perceptual-based Saturation-Brightness quantization are presented in Sections 4.2 to 4.5 .

4.2 Foreground Extraction and Background Removal using Dominant Colors

As previously mentioned, most coloration analysis images usually include a reference color strip to correct for non-standard illumination conditions. Since the color strip does not provide any useful information to the task of segmenting the area of interest, we choose to detect and remove the color strip from the image by cropping it. This helps to improve the computation time by reducing the number of pixels used for further processing. After color strip removal and image cropping, a foreground extraction process is implemented on the input image to remove background regions. The foreground-background extraction is performed by assigning each pixel in the image to either a background or foreground region (also referred to as class or cluster) based on the pixel color. This process is a two-class (background/foreground) color quantization of the image color space and can be achieved using any of the several color space segmentation approaches available in the literature such as mean-shift clustering [37], Gaussian mixture model based classification [38], k-means clustering [38], color

quantization methods used in display devices [39] etc. In this proposed work, the foreground–background classification is performed using a k-means clustering algorithm. However, it is well known that using an unsupervised k-means clustering approach is extremely sensitive to the choice of initial seeds (initial representative color for each cluster). Better results can be achieved by using user-provided or intelligently derived initial seeds as compared to a random selection of initial seeds [40]. In this work, we are interested in an automatic initial seed selection process rather than user-provided seeds. For this purpose, we propose the use of dominant colors in the image as the initial seeds for the k-means clustering.

4.2.1 Dominant color extraction in images

Ma et al. [41] proposed the idea of using dominant colors for a concise color space representation for image segmentation and a number of different approaches for dominant color extraction have been proposed [41]-[45]. In this work, the dominant colors in the image are automatically identified by computing the color distribution of the image content. The dominant colors are determined by locating local peaks or modes in the image color distribution using the mean-shift mode detection as in [37]. The use of a few important colors to represent the image color distribution helps in merging regions of similar color into a single abstraction that aids the task of ROI segmentation. Before computing the dominant colors in the image, the input image is convolved with a Gaussian smoothing filter in order to remove noise and merge very small regions of color with the nearest larger color cluster. This helps to reduce the number of unique colors in the image and speed up mode detection. Another approach to reduce the number of unique colors is to quantize an 8 bit three channel RGB image to a 5 bit three channel

image by ignoring the last 3 bits of every 8 bit pixel value in the image [39]. Such a preprocessing step can reduce the maximum number of unique colors possible in an RGB image from 256^3 to just 32^3 with very little loss in quality for the considered application.

An important factor that affects the color segmentation results is the choice of color spaces. As discussed in Chapter 2, the RGB color space is perceptually non-uniform, i.e., a small perceptual difference between two colors can correspond to a large distance in the color space and vice versa [22]. Since the Euclidean distances used to measure color differences in these non-perceptually uniform color spaces do not correspond to human perceived color differences, the RGB color space is not the best choice for image segmentation methods aimed at emulating human visual perception. It has been shown that the performance of color segmentation methods is greatly improved by using perceptually uniform color spaces such as the ones recommended by the CIE [46]. In this work, the perceptually uniform L*a*b* (also known as CIELAB) color space, described in Section 2.1.2 of Chapter 2, is used for representing the color distribution of the considered images as it provides a perceptually uniform representation of colors [37], [42], [46]. This helps to ensure that perceptually similar colors are grouped in the same segmentation class. Also, since the luminance L* and chrominance a*b* components in the L*a*b* color space are separated, we only need to consider the a* and b* color components for extracting the dominant colors in the image as compared to the R, G and B components in the RGB color space. This reduces the complexity of the dominant color extraction process as well as the k-means clustering process.

Fig. 8. Original image containing multiple colors.

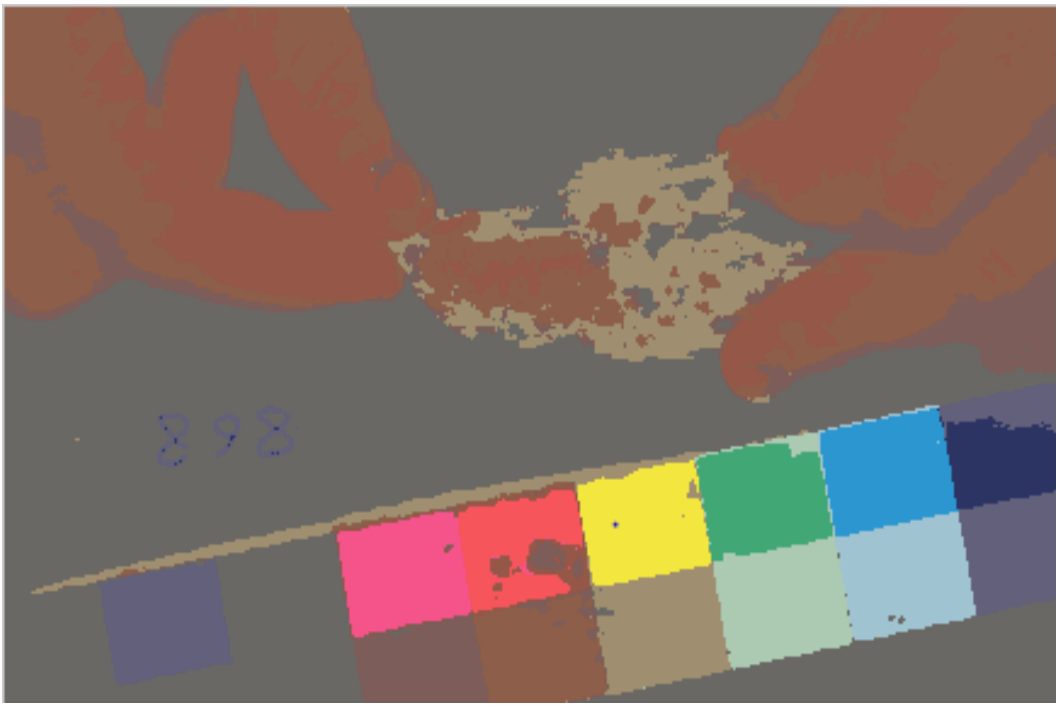

Fig. 9. Image Segmentation result using 14 dominant colors.

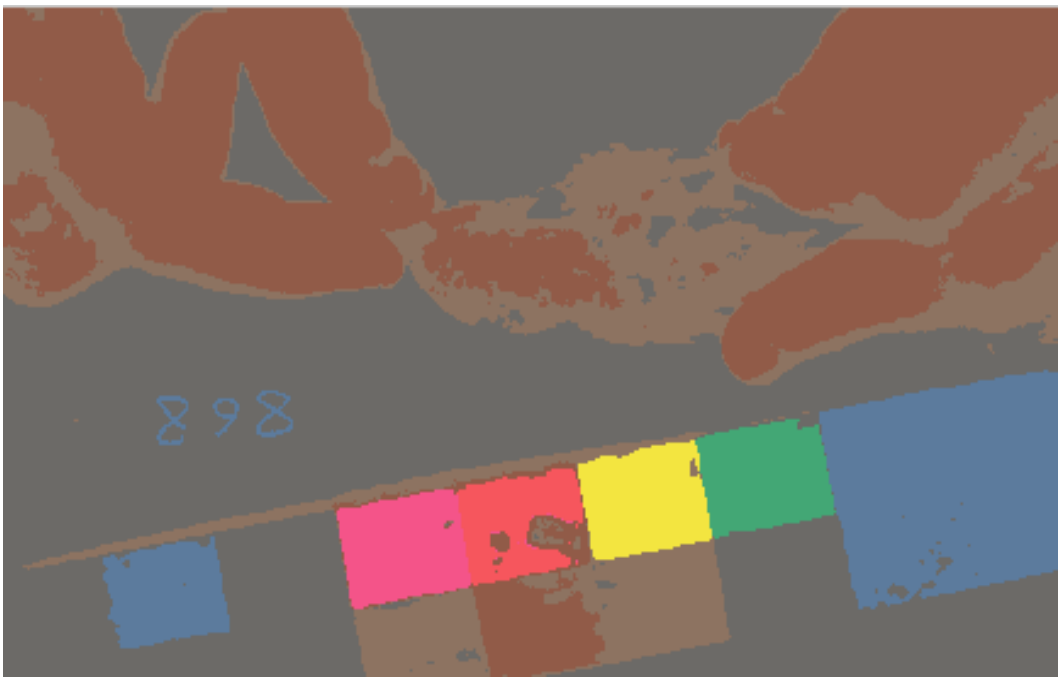

Fig. 10. Segmentation result using 8 dominant colors.

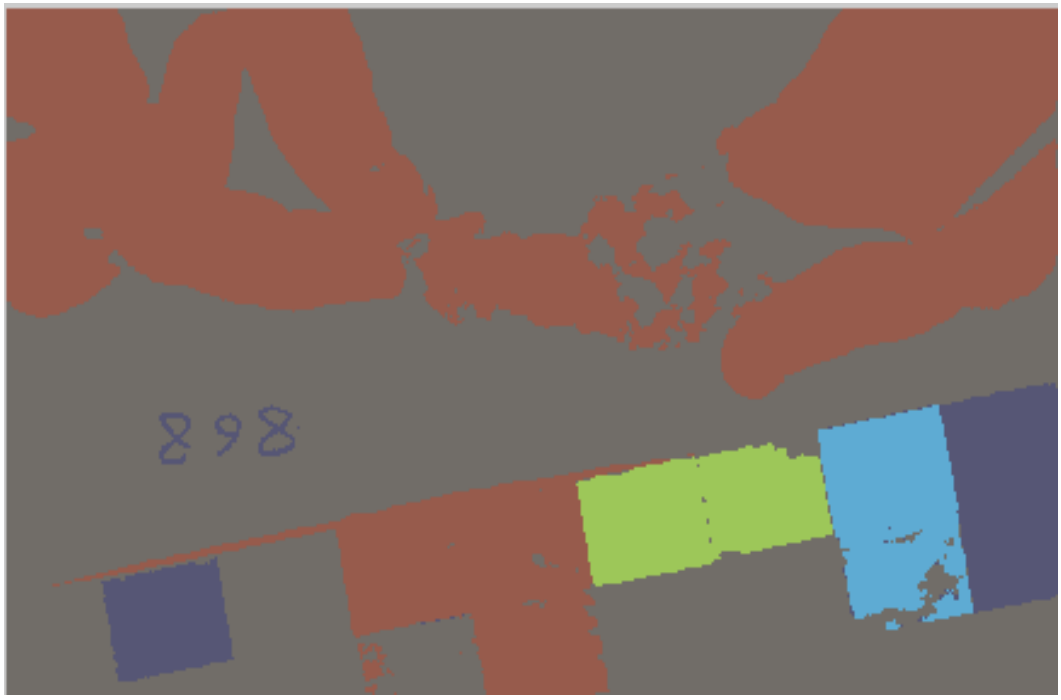

Fig. 11 Segmentation result using 5 dominant colors.

We first generate an L*a*b* space mapping of the colors in the image and then compute a 2-D color histogram of the image, where the chrominance components a* and b* represent the dimensions of the 2-D color histogram. The dominant colors are then determined by detecting modes (local peaks) in the histogram as indicated previously. The number of dominant colors detected also affects the accuracy of segmentation results. Using a large number of colors results in over-segmentation of the image, while using very few colors results in under-segmentation of the image and parts of the region of interest being assigned to the background class. In the proposed framework, the number of colors detected is adaptive and depends on the size of the window used for mode detection. The size of the window is chosen to be a factor of the total variance of the image color space. Fig. 8 shows the original image, while Fig. 9, Fig. 10 and Fig. 11 show image segmentation results using different number of dominant colors such as 14, 8 and 5 dominant colors, respectively.

4.2.2 Foreground extraction using k-means clustering

After extracting the dominant colors of the image, a k-means clustering operation is performed as described earlier, on the color values using the a* and b*component values for each pixel in the image to produce a multi-class abstraction of the image, with the number of classes produced being equal to the number of dominant colors detected previously. Since the background has an almost homogenous color and occupies the largest portion of the total image area, the background cluster is identified as the cluster whose center is closest to the largest peak in the image color distribution, which corresponds to the background dominant color. Pixels in a particular dominant color

Fig. 12. Input image.

Fig. 13. Foreground-background class abstraction for the image shown in Fig. 12; foreground region shown in white.

cluster are assigned to the background cluster based on how close their cluster center is to the background cluster center and this is evaluated by taking the Euclidean distance between the candidate cluster center and the identified background cluster center. All pixels in a cluster are labeled as background pixels, if the Euclidean distance between their cluster center and the background cluster center is less than a certain threshold. The value of the threshold used in this work is equal to 12. The remaining pixels are labeled as foreground pixels. This results in the segmentation of the image into a background region that is ignored and a foreground region that is processed further. Fig. 13 shows the

resulting foreground-background segmentation mask for the input image shown in Fig. 12, where the white and black regions correspond, respectively, to the extracted foreground and background regions.

4.3 Skin/Non Skin Region Classification

In images involving color quantification of live, fast moving animals, the specimen is held in position by human hands. Since we initially segment the image into just two classes, the region corresponding to human hands in the image may also be retained in the foreground class as shown in Fig. 13. Since no prior knowledge about the color of the ROI is assumed before the start of segmentation, a foreground - background classification based on dominant colors is not enough to accurately extract the ROI. In order to differentiate the ROI from the region corresponding to human hands in the image, the foreground class needs to be further segmented. We achieve this segmentation by first using a Bayesian skin color classifier [47], which segments the foreground class into candidate skin and non-skin pixels on the basis of chrominance values for each pixel.

In order to use the Bayesian classifier for human skin classification, we first need to estimate the class conditional probabilities from a sample dataset of skin and non-skin images. The conditional probability distributions for the skin and non-skin classes can be modeled each in color space as single bivariate Gaussian distributions as shown in [47], [48], [49] and as Gaussian mixture density models as shown in [49], [50], [51]. Two important factors for implementing an efficient skin detector are:

(i) The amount of overlap between the skin and non-skin distributions and the shape of the distributions in a given color space.

(ii) The ability of a probabilistic model to approximate a complex-shaped distribution in a given color space.

In the proposed framework, the perceptually uniform CIELAB (L*, a*, b*) space is used to model the skin and non-skin conditional densities. The skin color distribution in such perceptually uniform spaces usually takes the shape of a complex multi-modal distribution. To effectively model such a complex shaped distribution, a Gaussian mixture model is used in this framework. The Gaussian mixture model is estimated by implementing the approach mentioned in Section 2.2 on a sample data set consisting of 500 images of size 60x60 pixels each, with 250 images for the skin class and 250 images for the non-skin class. This results in a total of around 2 million pixel color values. The images are transformed to the CIELAB space and the Expectation-Maximization algorithm is implemented using the entire dataset. Fig. 14 shows sample images from the skin dataset.

The number of components in a Gaussian mixture model is usually assumed to be known. In general, increasing the number of parameters tends to increase the likelihood but also leads to over-fitting. To determine the exact number of components needed for a given data distribution, an information criteria such as the Akaike Information Criterion (AIC) or AIC with correction (AICc) can be used. Such information criteria assign a penalty term for the number of components to balance the tradeoff between maximizing the likelihood and over-fitting. The AIC gives the optimal number of components under asymptotic conditions. The AIC is given by the equation [52],

$$AIC = 2k - 2\ln(L) \tag{34}$$

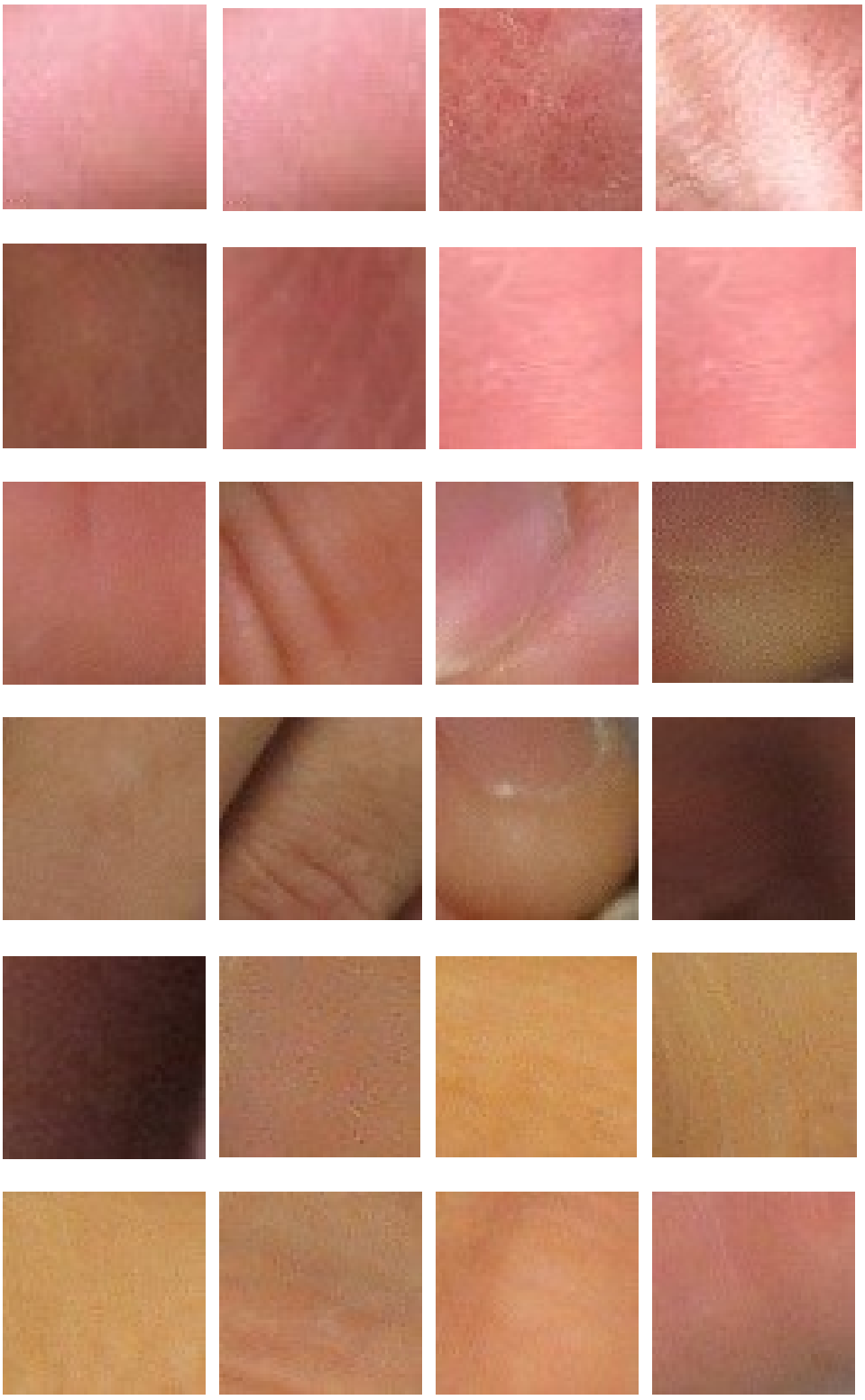

Fig. 14 Sample images from the skin dataset used to estimate the skin condition.

where k is the number of free parameters in the model and L is the maximized value of the likelihood function for the estimated model. For a Gaussian mixture model with M bivariate Gaussian components having symmetric non-diagonal covariance matrices, the number of free parameters $k = (6M - 1)$ [53]. The AIC is computed for a set of candidate models and the model that produces the minimum AIC value is chosen as the model with the optimal number of components [52]. For the skin color dataset used in this work, an 8 component Gaussian mixture model provided good results. As discussed in Section 2.2, the initial estimates for the mean vectors and covariance matrices of the Gaussian components are obtained by a vector quantization of the color space distribution. The skin class conditional can be obtained from (16) by choosing M=8 and is given by:

$$p(\bar{X}(i,j)|S = 1) = \sum_{i=1}^{8} w_i \; g(x|\mu_i, \Sigma_i) \tag{35}$$

where $g(x|\mu_i, \Sigma_i)$ is a bivariate Gaussian density function as described in (17), μ_i and Σ_i represent, respectively, the mean vector and covariance matrix, the vector $\bar{X}\,(i,j) = [a^*(i, j)\; b^*(i, j)]^T$ represents the chrominance values (a^*,b^*) for the pixel at coordinates (i, j) and S is used to represent the skin class for S=1 and the non-skin class for S=0. The non-skin distribution is modelled as a single bivariate Gaussian density function and is given by,

$$p(\bar{X}(i,j)|S = 0) = g(x|\mu_i, \Sigma_i) \tag{36}$$

where $g(x|\mu_i, \Sigma_i)$ is same as described in (17). The non-skin distribution can also be modelled as a Gaussian mixture model, but a single Gaussian provided good results for the tested images.

Using the class conditional densities defined earlier, a two class Bayesian classifier, as explained in Section 2.3 is implemented, and classifies every pixel in the foreground

class as skin or non-skin pixel. Given a chrominance vector $\bar{X}(i,j) = [a^*(i,j)\ b^*(i,j)]^T$ for an image pixel at coordinates (i, j), and assuming equal prior probabilities for both the skin and non-skin class, the classifier classifies this pixel as a skin pixel if,

$$p(\bar{X}(i,j)|S=1) \geq p(\bar{X}(i,j)|S=0) \tag{37}$$

A binary mask $S(i,j)$ is produced by the Bayesian classifier where $S(i,j)=1$ corresponds to a candidate skin pixel at location (i,j), and $S(i,j)=0$ corresponds to a non-skin pixel.

4.4 Edge-Enhanced Model-Based Classification for Outlier Pixel Removal

As mentioned in Section 4.3, the foreground region needs to be segmented into a skin and a non-skin class in order to remove the region corresponding to human hands in the foreground class. The accuracy of a human skin classifier based on chrominance only, largely depends on the amount of overlap between the class conditional densities of the skin and non-skin classes in the color space and the number of samples in each of the training sets for each class [49]. This thesis work focuses on a broad set of images consisting of different species of animals used in coloration analysis instead of a single species of animals. As a result, no assumption regarding the color of the specimen is made in this approach, except that the background is chosen to be different than the colors of interest of the animal. As illustrated in Fig. 12, it is possible that the color of the ROI is perceptually similar to the color of human hands. In such a case, the candidate skin pixels determined by the skin classifier might not all correspond to true skin pixels since some plumage colors might be similar to skin color and a skin color classifier may not be sufficient to effectively identify the ROI. To circumvent this problem, the candidate skin pixels that are obtained using the color-based Bayesian classifier are

further refined into skin and non-skin regions by using the edge information that is present in the luminance component of the considered image. Our model-based approach is based on the assumptions that 1) the region of human hands can be separated from an ROI having a perceptually similar color by using the luminance component of the image due to a perceivable difference in the luminance values of the hand region and the ROI, resulting in a significant or strong edge at the hand-ROI interface; and 2) the region of human hands is connected to the acquired image border as illustrated in Fig. 12. The first assumption helps in separating the similar colored hand region from the ROI if these are connected (Fig. 12). The second assumption helps in identifying and removing the hand region from the foreground. Removing directly the region connected to the border without initially separating the true hand region from the misclassified skin pixel regions in the ROI will result in the removal of parts of the ROI which are misclassified as skin pixel regions. Thus, in the proposed approach, an edge map is first generated and is used to separate the true hand region from the misclassified skin pixel regions in the ROI. The region that is connected to the image border is then determined as the true human hand region and removed from the foreground region in Fig. 13, resulting in the final ROI mask.

The Canny edge gradient operator [54] is used to first generate an edge gradient magnitude image. Other suitable edge detectors can also be used for this purpose. A binary edge map representing the strong edges in the image is generated from the edge gradient magnitude image using a thresholding operation. Pixels that form a strong edge are represented by a value of 1 in the binary edge map. We compute the threshold t_{high} for the Canny edge detector using a histogram of the edge gradient magnitudes. The

threshold t_{high} is chosen such that the top 10 percent edge gradient magnitude pixels in the histogram are marked as strong edges. For our application, we choose the top 10 percent pixels because we are only interested in the strong edges that are necessary to define object contours in the image. The low threshold t_{low} is computed exactly as defined by Canny in [54]. Fig. 15 illustrates the resulting binary edge map for the foreground region of the image shown in Fig. 13. The resulting binary edge map is then inverted to produce a binary mask $E(i,j)$. A point-by-point multiplication of $E(i,j)$ with $S(i,j)$, the binary mask produced by the Bayesian skin classifier, helps to split skin (hand) regions connected to the ROI:

$$F(i,j) = E(i,j) * S(i,j) \tag{38}$$

A refined region mask representing the human skin is generated, as illustrated in Fig. 16, by first removing regions connected to the image borders in *F(i,j)* and then subtracting the resultant mask from the original foreground region mask shown in Fig. 13. The final ROI mask (Fig. 17) can be obtained by subtracting the human skin mask (Fig. 16) from the original foreground mask (Fig. 13). Alternatively, the final ROI mask (Fig. 17) can be obtained by first removing regions connected to the image borders in *F(i,j)* and then multiplying the resultant mask with the foreground region mask (Fig. 13).

Fig. 15. Binary edge map.

Fig. 16. Hand region mask.

Fig. 17. Final generated ROI mask

4.5 Perceptual-based Saturation-Value Quantization

In some plumage coloration studies such as those for the house finches, researchers are interested in carotenoid based coloration and, for these applications, they usually do not include regions of the bird plumage that have shades of white, gray and black in the ROI used for analysis. These studies are targeted at measuring chrominance values of regions having colors like red, yellow, blue, green, to name a few, whose chrominance values are related to the amount of color producing carotenoid pigment present in the birds [1]. As previously discussed in Section 2.1.3, in the *HSV* (*H*: Hue, *S*: Saturation; *V*: Value) color space, the colors white, black and shades of gray can be produced for any value of hue (*H*), i.e., these colors are a function of only the saturation (*S*) and value (*V*) components. For example, black is produced when $V = 0$ and $0 \leq S \leq 1$ [25], the color white corresponds to the point (*S, V*) = (0, 1) in Saturation – Value space, while shades of gray are produced at all points along the vertical axis in *HSV* color space, i.e., when $S = 0$ and $0 \leq V \leq 1$ as shown in Fig. 18. Also the human ability to perceive vivid color diminishes as the brightness (V) decreases. As a result, at lower brightness levels, colors appear to be shades of gray or even black, even though $S \neq 0$ and $V \neq 0$. As the final step in this framework, a perceptual-based Saturation–Value quantization is proposed to exclude pixels that would be perceived to have a gray, black or white color if these colors are not of interest. The binary level quantization decision boundary shown in Fig. 19 is used to generate a binary mask as shown in Fig. 20, based on the *S* and *V* values. The binary mask is generated as follows:

$$B(i,j) = \begin{cases} 0, & S \leq 0.2 \text{ or } V \leq 0.15 \text{ or } V + S - 0.85 < 0 \\ 1, & \text{otherwise} \end{cases} \tag{39}$$

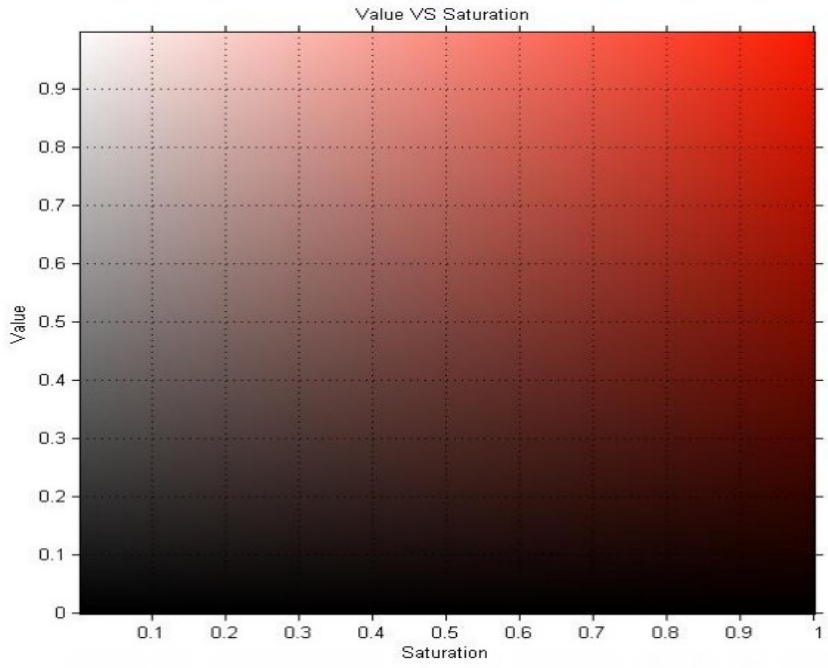

Fig. 18. Plot of Value versus Saturation for a single hue (Hue = 6º).

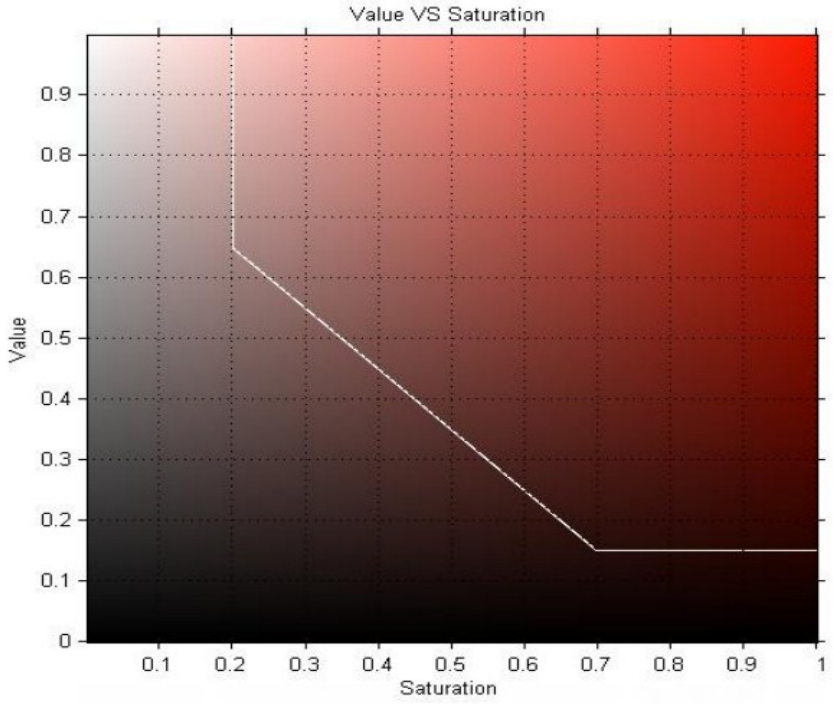

Fig. 19 Quantization decision boundary overlay on Value versus Saturation plot.

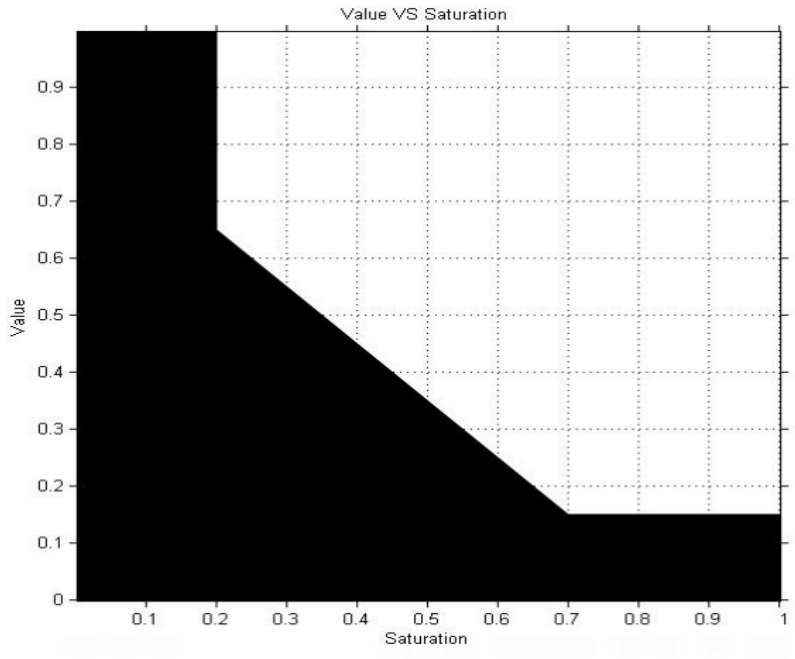

Fig. 20. Binary mask generated using perceptual-based Saturation-Value quantization.

where *B(i, j)* is the binary mask, {*S*=Saturation, *V*=Value} are the Saturation and Value intensities at point (*i, j*) in the image.

The black region in Fig. 20, corresponds to the region of (Saturation, Value) value pairs in Fig. 18 that would be considered as perceptually insignificant colors in some coloration studies, i.e. white, black and shades of gray color, while the white region in Fig. 20 represents the perceptually significant colors in Fig. 18. The white line in Fig. 19 represents the quantization decision boundary in (S, V) space. This decision level can be further adapted to the input image characteristics based on the range of colors and contrast present in the image. Fig. 21 illustrates the final ROI extracted using the proposed framework.

4.6 MATLAB-based Software Implementation.

A MATLAB-based software package implementing the proposed framework has also been designed and can be found here: http://ivulab.asu.edu/software/coloration/abcot . The software package provides an easy to use GUI for color quantification of image datasets. Fig. 22 shows the GUI for the MATLAB-based software package. The user can analyze just a single image using the single image option or an entire dataset of images using the batch processing option. The user can specify the presence and orientation of the color strip and the software package can process both, images in which a color strip is present and images in which a color strip is not present. The GUI also provides several options to customize the algorithm as per user needs. For example, if only the colors like black, gray and white need to be quantified, the user can disable the option of 'Perceptual Quantization' to avoid removal of these colors from the ROI. This way the software package can be used to quantify both melanin-based as well as carotenoid based colors. The 'Colors to Reject' option allows the user to calibrate the software package to always avoid certain colors from being included in color quantification. By choosing the 'Glove Reject' option, the user can also process images in which the animal is held by a human wearing gloves. The software package also provides the user to save customizable settings of the algorithm for future reuse. The user can also choose the output format for the color quantification results generated. In addition to a standard excel sheet which contains the mean and variance measurements for hue, saturation, value and patch size for each ROI along with the image name, the user can also save a binary image showing the selected ROI as shown in Fig. 17 and an image showing the outline of the final extracted ROI overlayed on the input image as shown in Fig. 21. These images can be

used to identify errors in ROI selection, which is not possible with current semi-automated methods as no image based evidence of the selected ROI is stored.

A summary of the major steps for the software implementation of the proposed framework is as follows:

Step 1: Perform Gaussian smoothing on input image and transform it from *RGB* color space to the perceptually uniform CIELAB (L^*,a^*,b^*)color space.

Step 2: Compute the 2-D color space histogram of the image using the chrominance components a^* and b^* as the two dimensions.

Step 3: Detect the peaks in the histogram computed in Step 2 to compute representative dominant colors.

Step 4: Perform k-means clustering in color space to extract the foreground and background region using as initial seeds the representative colors found in Step 3.

Step 5: Perform human skin classification using a Bayesian classifier on the foreground region and generate new mask representing candidate skin pixels.

Step 6: Extract and remove skin region using edge map and boundary of image.

Step 7: Use perceptual based Saturation-Value quantization to remove perceptually insignificant colors from ROI.

Step 8: Quantify colors in the ROI for each color patch in terms of color patch size, mean hue, mean saturation, and mean value.

Fig. 21. Outline of final extracted ROI overlayed on original image

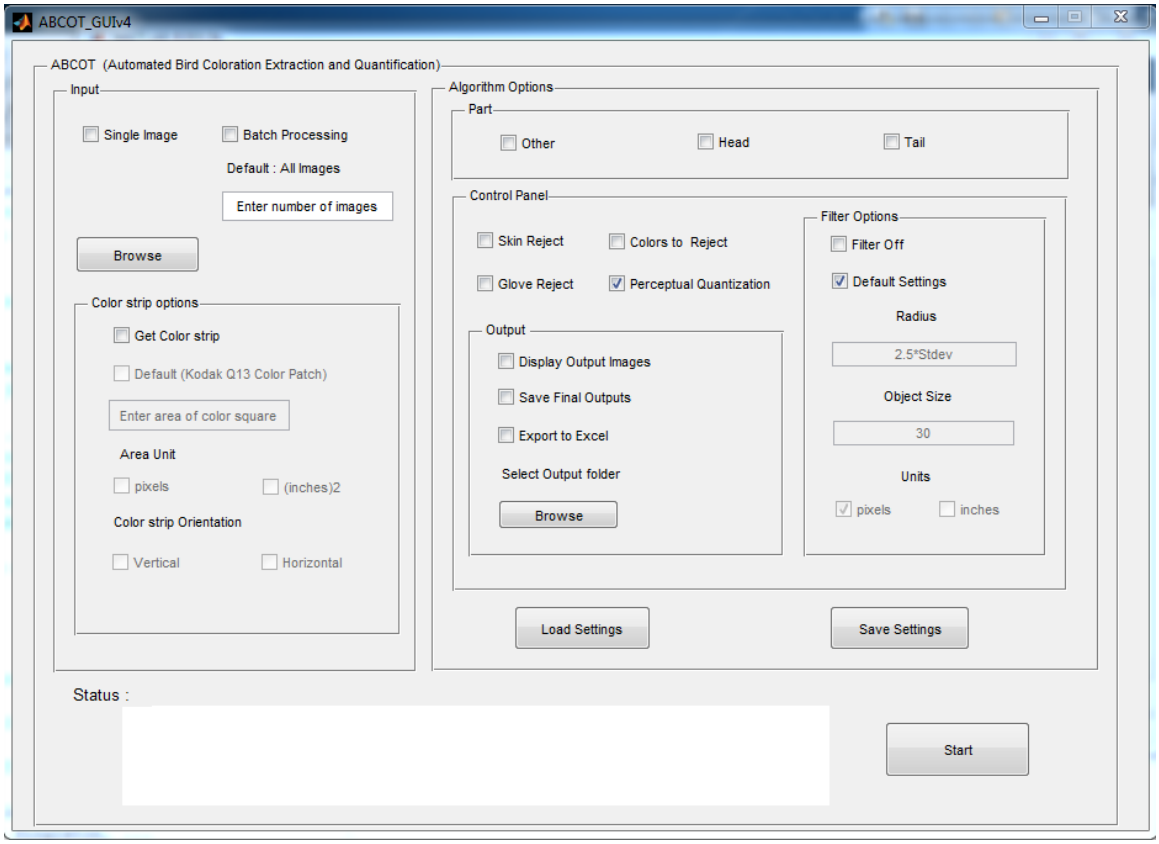

Fig. 22. User interface for MATLAB-based implementation of proposed method.

CHAPTER 5

EXPERIMENTAL RESULTS

In this chapter, the experimental results of the proposed framework for segmenting and quantifying animal coloration using different image sets, are presented and analyzed. Section 5.1 introduces the image sets used to evaluate the accuracy and repeatability of the implemented framework. Section 5.2 describes how the hand scored images for performance evaluation were obtained. Section 5.3 presents the inter-photo and intra-photo repeatability results for the measured hue, saturation, value and patch size for different image sets. Section 5.4 presents performance comparison results between hand-segmented and manually scored results and the results generated using the implemented framework.

5.1 Data Set Description

The inter-photo, intra-photo repeatability and linear correlation results are evaluated for two datasets, the rump image dataset and the breast image dataset. Dataset 1 (rump image dataset) is generated by taking images of the rump region of different specimens of the house finch (*Haemorhous mexicanus*). It consists of images of 33 different specimens, consisting of both juvenile and adult specimens. Two images are generated for each of the 33 different specimens to check for inter-photo repeatability. For each specimen, the two images generated differ slightly in terms of illumination, position of the bird and camera zoom. In total, Dataset 1 has 66 images and, in each image, the bird is held in place by human hands with a standardized color strip placed next to the specimen to correct for non-standard illumination conditions. Fig. 23 shows sample images from

Fig. 23 Example images from the rump dataset (Dataset 1).

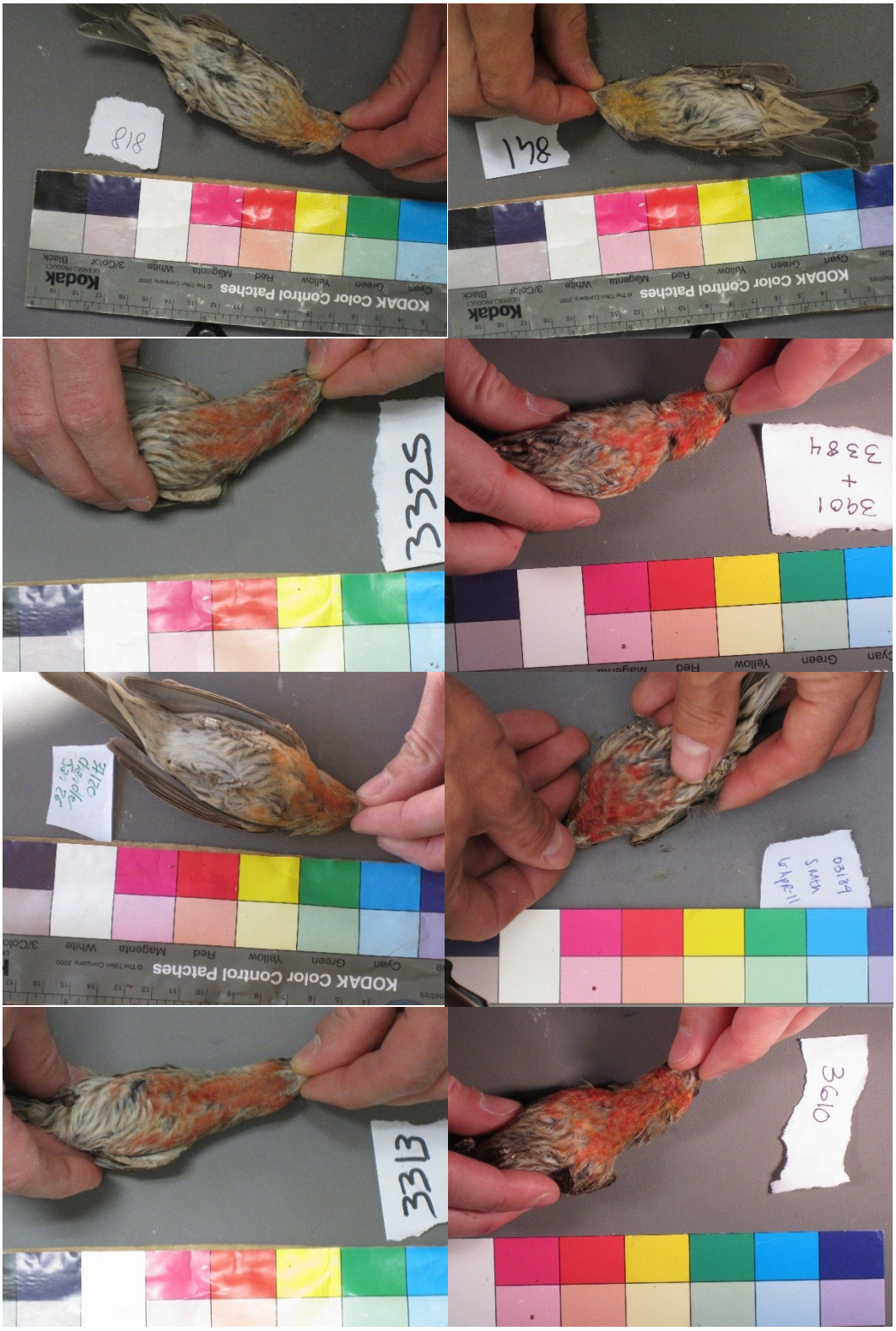

Fig. 24 Example images from the breast dataset (Dataset 2).

Dataset 1. Dataset 2 (breast image dataset) is generated by taking images of the breast region of different specimens of the house finch (*Haemorhous mexicanus*). Similar to Dataset 1, Dataset 2 (breast image dataset) consists of images of 25 different specimens. Just like Dataset 1, two images are also generated for each of the 25 different specimens to check for inter-photo repeatability, and the two images generated differ slightly in terms of illumination, position of the bird and camera zoom. Dataset 2 has a total of 50 images and in each image the bird is held in place by human hands with a standardized color strip placed next to the specimen to correct for non-standard illumination conditions. Fig. 24 shows example images from Dataset 2.

5.2 Manual Results Generation

In order to evaluate the performance of the proposed automated quantification method, hand scored results need to be generated for all images in Dataset 1 and Dataset 2. These hand scored results are generated by using a semi-automated software based method using the freely available photo editing software GIMP [33]. The photos from each dataset are imported in GIMP and the region of interest is selected by a user for each image using a custom-written plugin in GIMP. The custom-written plugin uses the fuzzy select region selection tool in GIMP to enable the user to select the region of interest. This built in region selection tool in GIMP is similar to the magic wand region selection tool in Adobe Photoshop [32]. This tool uses a region growing method as explained in 3.1, where the user provides the initial seed location in the image and controls the region growing process by adjusting a threshold. The region growing method uses similarity of color to control the region growing and the user defined threshold controls how similar a candidate region color should be, in order to be merged with the parent region. The

GIMP plugin allows the user to repeatedly adjust the region growing threshold until the user is satisfied with the region selected. After the user is satisfied with the region selected, the plugin generates a binary mask of the region selection, where pixels in the selected region are denoted by a value of 1 and all other pixels are set to a value of zero.

The binary masks generated for all images in Dataset 1 and Dataset 2 are then imported into Matlab along with the original images in the two datasets to compute the average hue, average saturation, average value and patch size for each ROI. These values are computed by performing a point-by-point multiplication of each channel of the original image in HSV color space with its corresponding binary mask, followed by a mean computation step where all the pixels in the selected region are used to compute the mean hue, saturation and value. For each image, a set of four values is generated. These values are then further used for performance analysis as explained in 5.3 and 5.4.

5.3 Inter-photo and Intra Photo Repeatability

The inter-photo repeatability is evaluated by computing the repeatability of results between each pair of images for all 33 specimens in Dataset 1 and 25 specimens in Dataset 2 to judge the similarity between the regions of interest identified by the proposed scheme for two images of the same specimen with slightly different illumination conditions, position of the specimen and camera zoom. Ideally the inter-photo repeatability value should be close to 100%, as the exact same specimen is photographed in both images with slight differences in image acquisition conditions, as explained earlier in Section 5.1. Similarly, the intra-photo repeatability is evaluated by computing repeatability results between a pair of exactly identical images for all specimens in Dataset 1 and Dataset 2. The intra-photo repeatability helps to judge the

similarity between the regions of interest identified by the software as well as the human observers for a pair of identical images, which are scored a few days apart. Since, the same images are being scored on different days, the intra-photo repeatability should ideally be equal to 100%

The repeatability is computed as the intra class correlation coefficient as stated in [55]. The intra class correlation coefficient *r*, can be computed using most common statistical packages and is obtained as follows [55]:

$$r = \frac{S_A^2}{(S_w^2 + S_A^2)} \tag{40}$$

where, S_A^2 is the among-groups variance component and S_w^2 is the within-group variance component. The above mentioned variance components can be computed by using a one-way analysis of variance (ANOVA). Here we provide the general equations to compute the repeatability *r* using ANOVA [56]:

$$S_w^2 = MS_w \tag{41}$$

$$S_A^2 = (MS_A - MS_w)/n_0 \tag{42}$$

$$n_0 = \left[\frac{1}{K-1}\right] * \left[\sum_{i=1}^{K} n_i - \left(\sum_{i=1}^{K} n_i^2 \,/\, \sum_{i=1}^{K} n_i\right)\right] \tag{43}$$

where, *K* is the total number of groups, n_i is the number of samples in each group, MS_w represents the mean squares within groups and MS_A represents the mean squares among-groups in the ANOVA table. The mean squares are computed using the sum of squares measure for within groups SS_W and among-groups SS_A using the following equations [55],

$$MS_w = \frac{SS_W}{df_W} \tag{44}$$

$$MS_A = \frac{SS_A}{df_A} \tag{45}$$

where df_W and df_A represent the within group and among-group degrees of freedom. The mean squares in ANOVA is equal to the sum of squares measure divided by the degrees of freedom. The degrees of freedom are obtained as follows,

$$df_A = K - 1 \tag{46}$$

$$df_w = df_{total} - df_A \tag{47}$$

$$df_{total} = N - 1 \tag{48}$$

where K is the number of groups and N is the total number of measurements in the experiment. The sum of squares are computed as shown [55],

$$SS_w = \sum_{j=1}^{K} \sum_{i=1}^{n} (y_{i,j} - \mu_j)^2 \tag{49}$$

$$SS_A = \sum_{j=1}^{K} n * (\mu_j - \mu)^2 \tag{50}$$

where K is number of groups, n is the samples per group, $y_{i,j}$ is the measurement of sample i in group j, μ_j is the mean for group j and μ is the mean of all the N measurements and is also called the grand mean. Using the mean squares the F ratio is computed as follows,

$$F = \frac{MS_A}{MS_w} \tag{51}$$

The total variance is computed as the sum of the within group variance component and the among-group variance component.

For our inter-photo repeatability experiment, we define 33 groups for Dataset 1 and 25 groups for Dataset 2. Each group contains 2 images (samples) of the same specimen obtained under slightly different illumination conditions, position of specimen and camera zoom. Each group represents one specimen. So for the inter-photo repeatability experiment, K=33, n=2, N=66 for Dataset 1 and similarly K=25, n=2, N=50

for Dataset 2, where *K, n* and *N* are same as defined in equation (45). Similarly, for the intra-photo repeatability experiment, we define 33 groups for Dataset 1 and 25 groups for Dataset 2. Each group contains a pair of identical images, unlike the inter-photo repeatability experiment. The values for parameters *K, n* and *N* are same as those for the inter-photo repeatability experiment. The within group variance represents the variation due to image acquisition conditions and software, while the among-group variance represents the variation due to differences in the plumage colors of the individual specimens.

Using equation (36), the repeatability is computed for results generated using the proposed scheme and the hand-scored results generated by three users for images of Dataset 1 and Dataset 2. For each group of images, the repeatability is computed for 4 measured quantification parameters: average hue, average saturation, average value and patch size. The statistical analysis package JMP was used to compute the repeatability and generate the associated ANOVA tables. The evaluated inter-photo and intra-photo repeatability for the user-scored results and the results generated using the proposed scheme for all 4 measured quantification parameters for Dataset 1 and Dataset 2 is shown in Tables 1-4, respectively. The inter-photo repeatability variance components and the associated ANOVA tables for the measured hue, saturation, value and patch size results of the proposed scheme, user 1, user 2 and user 3 are shown in the Appendix A, Tables A1-A8, respectively, for Dataset 1. Similarly, these values for Dataset 2 are shown in Appendix A, Tables A9-A16.

Table 1. Inter-photo Repeatability of software and hand scored results for Dataset 1.

Method	**Repeatability for hue**	**Repeatability for saturation**	**Repeatability for value**	**Repeatability for patch size**
Proposed method	99.8%	99.5%	99.8%	98.8%
User 1	99%	89.7%	96.7%	78.8%
User 2	98.6%	89.9%	97.3%	86.8%
User 3	94.4%	74.4%	93.8%	39.9%

Table 2. Inter-photo Repeatability of software and hand scored results for Dataset 2.

Method	**Repeatability for hue**	**Repeatability for saturation**	**Repeatability for value**	**Repeatability for patch size**
Proposed method	99.98%	99.8%	100%	99.8%
User 1	98.3%	86.3%	97.7%	70.4%
User 2	98.2%	88.1%	98.8%	87.4%
User 3	98.1%	84.2%	97.3%	57.6%

Table 3. Intra-photo Repeatability of software and hand scored results for Dataset 1.

Method	**Repeatability for hue**	**Repeatability for saturation**	**Repeatability for value**	**Repeatability for patch size**
Proposed method	100%	100%	100%	100%
User 1	98.9%	92.2%	97.7%	97%
User 2	98.9%	87.3%	97.9%	87.6%
User 3	97.7%	85.5%	95.3%	89.9%

Table 4. Intra-photo Repeatability of software and hand scored results for Dataset 2.

Method	**Repeatability for hue**	**Repeatability for saturation**	**Repeatability for value**	**Repeatability for patch size**
Proposed method	100%	100%	100%	100%
User 1	99.2%	95.7%	99.5%	96.1%
User 2	98.6%	77.8%	98.2%	75.6%
User 3	97.9%	81.4%	96.6%	77.3%

The inter-photo repeatability values for Dataset 1 and Dataset 2 in Table 1 and Table 2 clearly show that the automated software framework generates results that provide much more repeatable values of the 4 measured quantification parameters as compared to hand scored results generated using current manual methods. The inter-photo repeatability of the proposed scheme is very close to the ideal value of 100% as compared to the user scored results. The intra-photo repeatability values in Table 3 and

Table 4 show that the proposed method produces results that are identical for pairs of identical images scored a few days apart. However, the user scored results for the same pairs of identical images are not identical and this proves that the proposed method produces much more repeatable results as compared to manual scoring methods.

5.4 Correlation Analysis of the Proposed Framework

The correlation analysis of the proposed framework is evaluated by computing the linear correlation coefficient between results generated using proposed method and user-scored results. The Pearson's correlation coefficient is computed for quantifying the correlation between the results generated using the proposed framework and user scored results. The correlation coefficient between two random variables X and Y with means μ_x , μ_y and variances σ_x^2 , σ_y^2 respectively is given as,

$$\rho(X,Y) = \frac{E[(X-\mu_x)(Y-\mu_y)]}{\sigma_X \sigma_Y} \tag{52}$$

Hand segmented ROIs are generated for all 33 specimens in dataset 1 and 25 specimens in dataset 2 by three different users as explained in 5.2. The correlation coefficient is computed between proposed method and user 1, proposed method and user 2 and proposed method and user 3, for all the four measured quantification parameters. The correlation coefficients for dataset 1 and dataset 2 are shown in Table 5 and Table 6 respectively. The proposed framework shows very strong correlation with all user scored results for the measured hue and value of the region of interest. The correlation between the proposed automated method and the manual scoring method is weaker for the measured saturation and patch size. This is due to the low inter-photo and intra-photo repeatability of manual scored results for saturation and patch size as compared to the

Table 5. Linear correlation of proposed method with user scored results for Dataset 1.

Correlation Pair	Hue	Saturation	Value	Patch size
Proposed method to user 1	0.9975	0.9063	0.9729	0.7768
Proposed method to user 2	0.9711	0.8160	0.9807	0.4832
Proposed method to user 3	0.9863	0.8364	0.9738	0.7023
User 1 to User 2	0.9699	0.8863	0.9816	0.6976
User 2 to User 3	0.9844	0.9024	0.9759	0.7120
User 1 to User 3	0.9864	0.8911	0.9807	0.8242

Table 6. Linear correlation of proposed method with user scored results for Dataset 2.

Correlation Pair	Hue	Saturation	Value	Patch size
Proposed method to user 1	0.9887	0.8335	0.9668	0.8124
Proposed method to user 2	0.9845	0.8227	0.9710	0.8301
Proposed method to user 3	0.9903	0.8969	0.9744	0.8764
User 1 to User 2	0.9870	0.8840	0.9861	0.8747
User 2 to User 3	0.9898	0.9120	0.9858	0.9292
User 1 to User 3	0.9864	0.8795	0.9893	0.8543

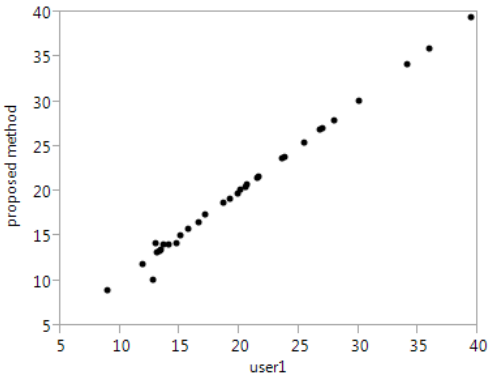

(a) Correlation Coefficient $\rho = 0.9975$

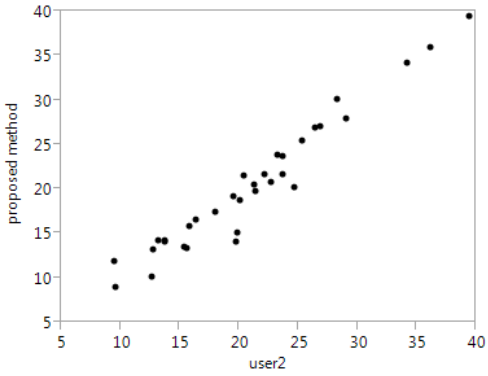

(b) Correlation Coefficient $\rho = 0.9711$

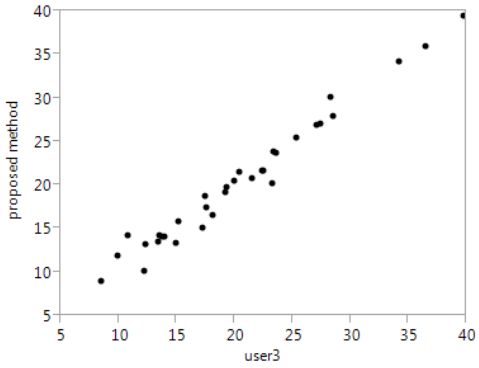

(c) Correlation Coefficient $\rho = 0.9863$

Fig. 25 Correlation scatter plots for measured hue of Dataset 1. (a) Relation between proposed method and user 1. (b) Relation between proposed method and user 2. (c) Relation between proposed method and user 3.

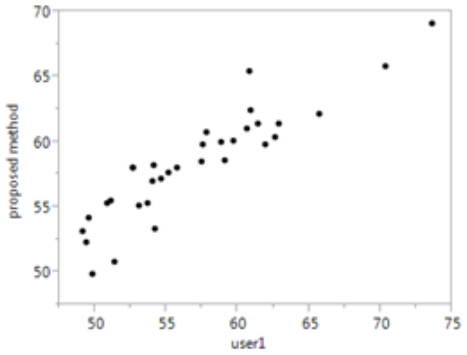

(a) Correlation Coefficient $\rho = 0.9063$

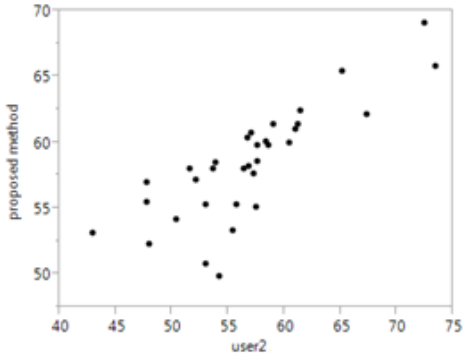

(b) Correlation Coefficient $\rho = 0.8160$

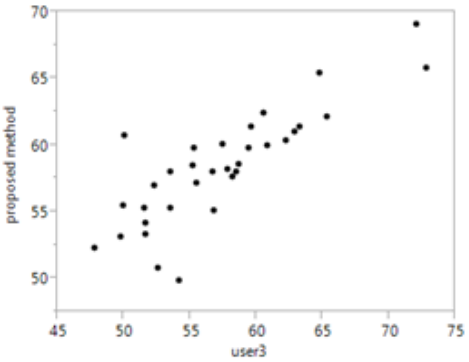

(c) Correlation Coefficient $\rho = 0.8364$

Fig.26 Correlation scatter plots for measured saturation of Dataset 1. (a) Relation between proposed method and user 1. (b) Relation between proposed method and user 2. (c) Relation between proposed method and user 3.

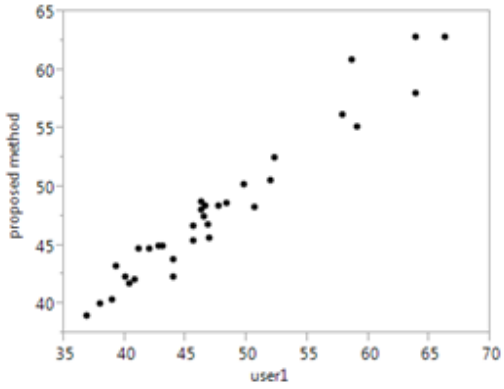

(a) Correlation Coefficient $\rho = 0.9729$

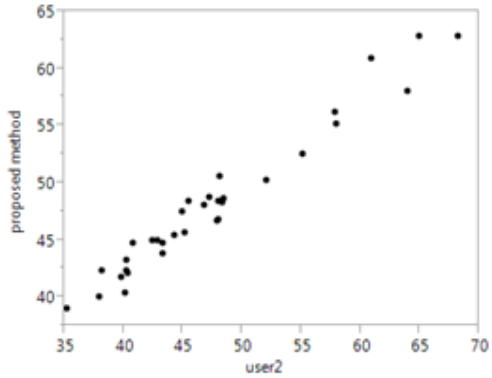

(b) Correlation Coefficient $\rho = 0.9807$

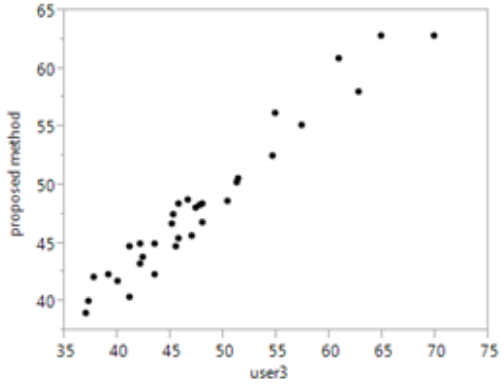

(c) Correlation Coefficient $\rho = 0.9738$

Fig. 27 Correlation scatter plots for measured value of Dataset 1. (a) Relation between proposed method and user 1. (b) Relation between proposed method and user 2. (c) Relation between proposed method and user 3.

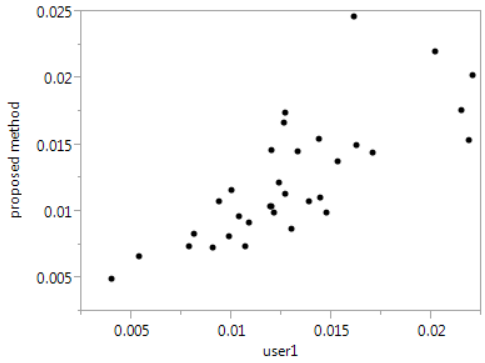

(a) Correlation Coefficient $\rho = 0.7768$

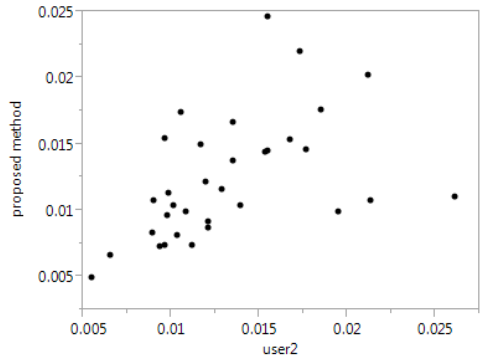

(b) Correlation Coefficient $\rho = 0.4832$

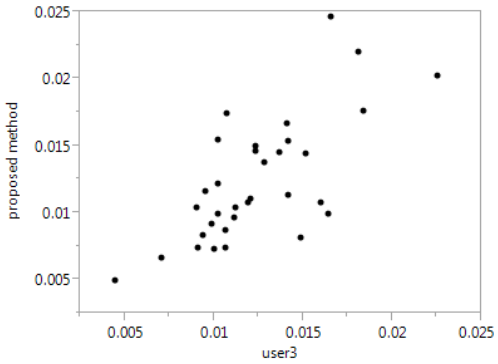

(c) Correlation Coefficient $\rho = 0.7023$

Fig. 28 Correlation scatter plots for measured patch size of Dataset 1. (a) Relation between proposed method and user 1. (b) Relation between proposed method and user 2. (c) Relation between proposed method and user 3.

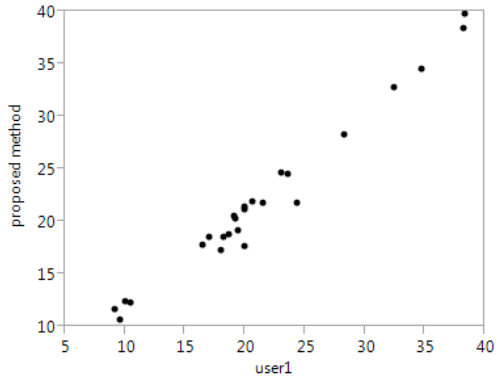

(a) Correlation Coefficient $\rho = 0.9887$

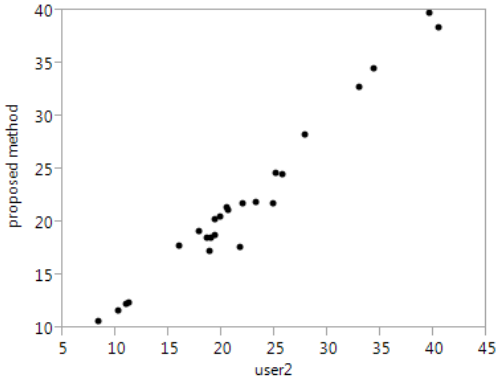

(b) Correlation Coefficient $\rho = 0.9845$

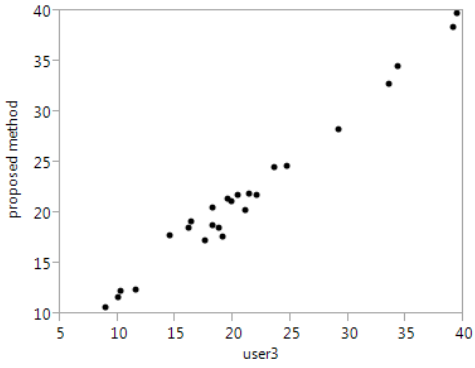

(c) Correlation Coefficient $\rho = 0.9903$

Fig. 29 Correlation scatter plots for measured hue of Dataset 2. (a) Relation between proposed method and user 1. (b) Relation between proposed method and user 2. (c) Relation between proposed method and user 3.

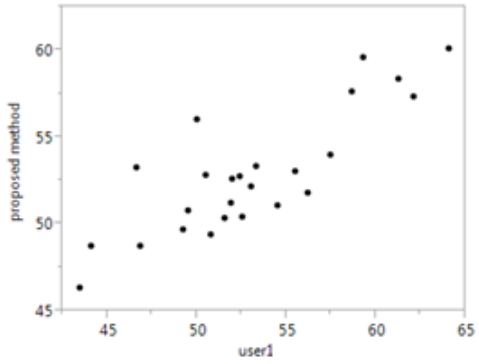

(a) Correlation Coefficient $\rho = 0.8335$

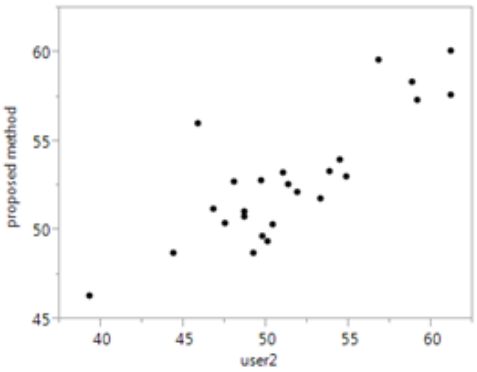

(b) Correlation Coefficient $\rho = 0.8227$

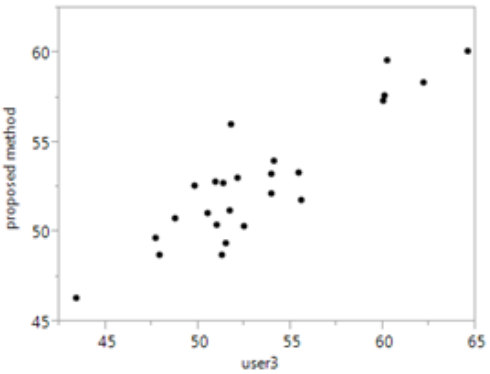

(c) Correlation Coefficient $\rho = 0.8969$

Fig. 30 Correlation scatter plots for measured saturation of Dataset 2. (a) Relation between proposed method and user 1. (b) Relation between proposed method and user 2. (c) Relation between proposed method and user 3.

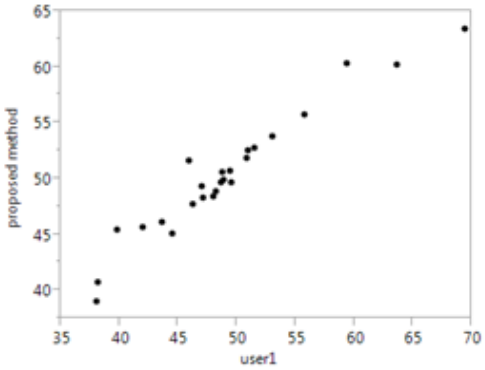

(a) Correlation Coefficient $\rho = 0.9668$

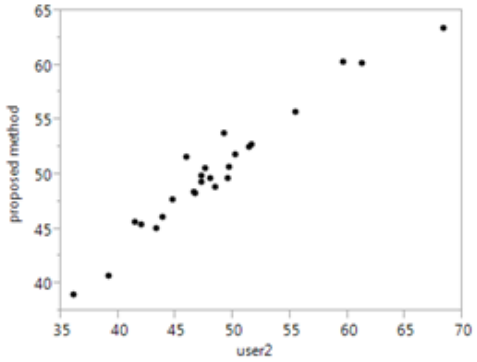

(b) Correlation Coefficient $\rho = 0.9710$

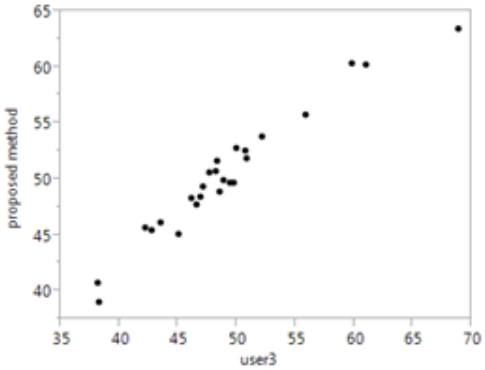

(c) Correlation Coefficient $\rho = 0.9774$

Fig. 31 Correlation scatter plots for measured value of Dataset 2. (a) Relation between proposed method and user 1. (b) Relation between proposed method and user 2. (c) Relation between proposed method and user 3.

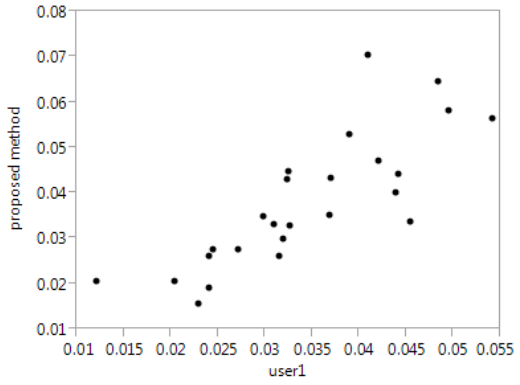

(a) Correlation Coefficient $\rho = 0.8124$

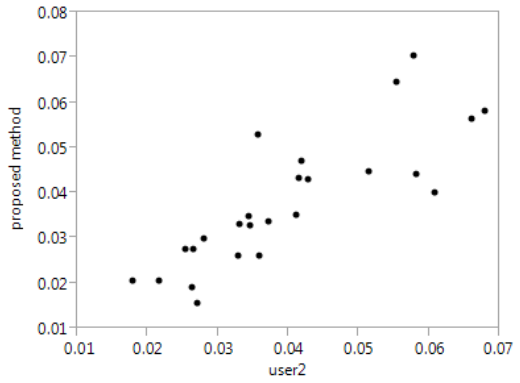

(b) Correlation Coefficient $\rho = 0.8301$

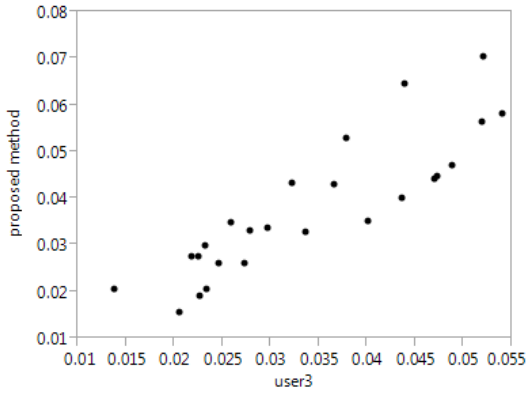

(c) Correlation Coefficient $\rho = 0.8764$

Fig. 32 Correlation scatter plots for measured patch size of Dataset 2. (a) Relation between proposed method and user 1. (b) Relation between proposed method and user 2. (c) Relation between proposed method and user 3.

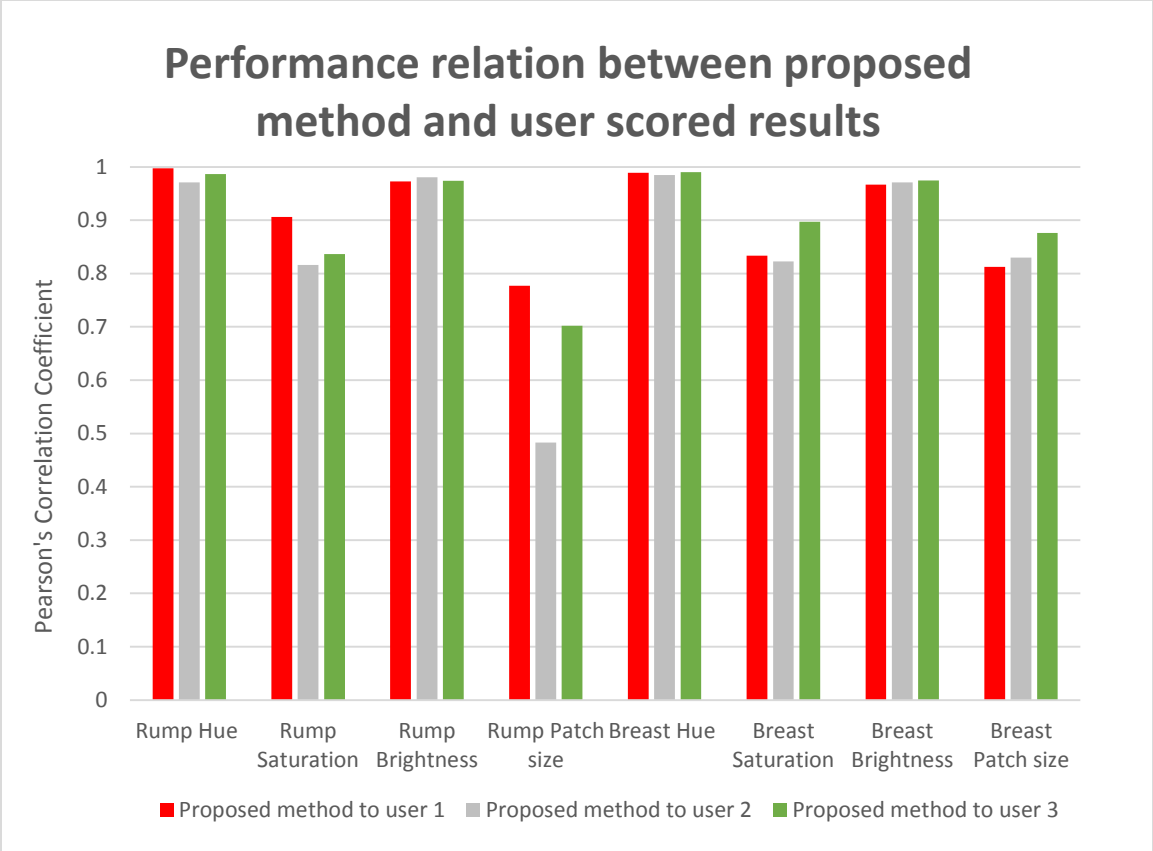

Fig. 33 Performance relationship between results generated using proposed scheme and user scored results for dataset 1 and dataset 2.

repeatability of the automated method for the same. The low repeatability of measured saturation is directly related to the low repeatability of measured patch size. Human observers tend to include pixels in the ROI based on the difference between the perceived color, brightness of a small region of pixels and its neighborhood in the image. There can be significant variation in the way the human visual system identifies such a region of pixels and its corresponding neighborhood depending on the image zoom during ROI selection and this results in the variation observed in the measured patch size. The variance of the saturation value of all pixels in the plumage region of the birds is much

higher than the variance of the hue and value of the same pixels. As a result, a variation in the measured patch size produces a much higher variation in the average saturation measurement for the ROI as compared to the average hue and value measurement for the same ROI. This reduces the repeatability of the measured saturation. On the other hand, the proposed framework relies on local pixel level color and brightness differences to identify the pixels in the ROI. This helps to reduce variation in the patch size of the selected ROI and in turn improves the repeatability of hue, saturation and value measurements.

Figs. 25-28 illustrate the relation between the proposed method and user scored results of images in dataset 1, for all the four measured parameters. Similarly, Figs. 29-32 illustrate the relation between the proposed method and user scored results of images in dataset 2, for all the four measured parameters. The performance relationship of the proposed method with user scored results for dataset 1 and dataset 2 is shown in Fig. 33.

CHAPTER 6

CONCLUSION

This thesis implements a framework for automated quantification of animal coloration in digital images. This work contributes to the field of image segmentation in general and to the area of animal color quantification in particular. This chapter summarizes the contributions of this thesis and proposes several directions for future research.

6.1 Contributions

In this thesis, a novel method that automatically segments and quantifies an animal color region of interest in digital images, is developed and implemented. The contributions of the thesis can be summarized as follows:

- A novel perceptual-based approach for the segmentation of animal coloration and its quantification using variables such as hue, saturation, brightness, patch size etc., in digital images with slowly varying background colors is presented.
- A novel perceptual-based Saturation-Brightness quantization is implemented for the removal of perceptually insignificant colors and only retaining the bright colors of interest
- This work develops a framework for segmenting the animal color region of interest by coarsely segmenting the image into foreground and background regions using dominant color quantization and then refining the foreground using skin pixel classification and a perceptual based Saturation-Brightness quantization scheme.

- The proposed framework produces much more repeatable and accurate results as compared to existing user-driven manual methods and also avoids the inter-observer error produced during manual scoring of results.
- The proposed method is much faster than existing user-based manual approaches and also produces results that are consistent with hand scored results. It takes an observer around 2-3 minutes to select an ROI using the manual methods while the software produces the result in less than 20 sec.

6.2 Future Research Directions

Possible enhancements to the proposed approach and future directions of research include the following:

- Incorporate robust background subtraction – The current work focuses on using images that have slowly varying background color. The work needs to be extended in the future to be able to process images acquired out in the field with variation in background illumination and presence of texture and other structures in background.
- Use of non-human color spaces – The color space used for color quantification in the proposed framework (*H, S, V*) is human based. Since, humans cannot perceive colors that lie outside the visible spectrum, human-based color spaces may not be a good choice for color quantification in certain applications. Although, humans are unable to perceive colors that lie in the UV spectrum, many animal species, especially birds have the ability to perceive colors in the UV spectrum. Since color signals are used by animals to attract prey, produce camouflage to hide from predators or attract mates

for breeding, it is important to incorporate non-human animal-based color spaces of the target receivers to understand the role of animal colors in these applications.

- Improve the algorithm to incorporate some sort of prior information about the specimen in the image to be able to segment complex color traits such as those found in chameleons, butterflies etc. and extend the scope of the algorithm to even perform recognition or classification based on such traits.
- Implement an adaptive Saturation-Brightness quantization scheme that assigns a pixel to the ROI by considering not only its own Saturation and Brightness values but also of the neighboring pixels.
- The proposed method is currently being used to extract color traits of birds, butterflies and reptiles. This work can be extended to target more difficult challenges like disease detection in animal species and population/species classification.

REFERENCES

[1] E. H. Paxton, "The Utility of Plumage Coloration for Taxonomic and Ecological Studies," *The Open Ornithology Journal*, vol. 2, pp. 17-23., 2009.

[2] M. Stevens, C. A. Parraga, I. C. Cuthill, J. C. Partridge and T. S. Troscianko, "Using Digital Photography to Study Animal Coloration," *Biological Journal of the Linnean Society,* vol. 90, pp. 211-237, 2007.

[3] K. J. McGraw, "Mechanics of melanin-based coloration," in *Hill GE, McGraw KJ, Eds. Bird Coloration: Mechanisms and Measurements*, vol. 1, Cambridge: Harvard University Press, 2006, pp. 243-294.

[4] K. J. McGraw, "Mechanics of Carotenoid-based coloration," in *Hill GE, McGraw KJ, Eds. Bird Coloration: Mechanisms and Measurements*, vol. 1, Cambridge: Harvard University Press, 2006, pp. 177-242.

[5] G. E. Hill, "Ornamental traits as indicators of environmental health," *Bioscience,* vol. 45, pp. 25-31, 1995.

[6] N. Johnson and R. Jones, "A new species of tody-tyrant (Tyrannidae: Poecilotriccus) from northern Peru," *Auk,* vol. 118, pp. 334-41, 2001.

[7] M. Stevens, M. C. Stoddard and J. P. Higham, "Studying primate color: towards visual system-dependent methods," *International Journal of Primatology,* vol. 30, no. 6, pp. 893-917., 2009

[8] F. B. Bercovitch, "Testicular function and scrotal colouration in patas monkeys.," *Journal of Zoology,* vol. 239, pp. 93-100, 1996.

[9] L. A. Isbell, "Seasonal and social correlates of changes in hair, skin, and scrotal condition in vervet monkeys (Cercopithecus aethiops) of Amboseli National Park, Kenya," *American Journal of Primatology,* vol. 36, pp. 61-70, 1995.

[10] J. M. Setchell and A. F. Dixson, "Changes in the secondary sexual adornments of male Mandrills (Mandrillus sphinx) are associated with gain and loss of alpha status," *Hormones and Behavior,* vol. 39, pp. 177-184, 2001

[11] S. Andersson and M. Prager, "Quantifying colors," in *In G. E. Hill & K. J. McGraw (Eds.),Bird coloration vol. I: Mechanisms & measurements*, Cambridge, MA, Harvard University Press, 2006, pp. 41–89.

[12] W. S and R. C., Computational colour science using MATLAB, Chichester: John Wiley & Sons, 2004.

[13] A. Alsam and R. Lenz, "Calibrating color cameras using metameric blacks," *JOSA A,* vol. 24, no. 1, pp. 11-17., 2007.

[14] P. Ferns and S. Hinsley, "Immaculate tits: head plumage pattern as an indicator of quality in birds," *Animal Behaviour,* vol. 67, pp. 261-272., 2004.

[15] M. Vanacova and P. Adamik, "Feather ornaments are dynamic traits in the Great Tit Parus major," *Ibis,* vol. 153, pp. 357-362, 2011.

[16] B. Matysiokova and V. Remes, "Egg yolk antioxidant deposition as a function of parentalornamentation, age, and environment in great tits.," *Journal of Avian Biology,* vol. 43, pp. 387-396, 2010.

[17] K. J.McGraw and G. E. Hill., "Plumage brightness and breeding-season dominance in the house finch: a negatively correlated handicap?," *Condor,* vol. 102, pp. 457-462., 2000.

[18] K. J. McGraw, A. M. Stoehr, P. M. Nolan and G. E. Hill, "Plumage redness predicts breeding onset and reproductive success in the house finch: a validation of Darwin's theory," *J. Avian Biol.,* vol. 32, pp. 90-94, 2001.

[19] K. J. McGraw and G. E. Hill, "Carotenoid-based ornamentation and status signaling in the house finch," *Behavioral Ecology,* vol. 11, no. 5, pp. 520-527, 2000.

[20] K. J. McGraw, P. M. Nolan, A. M. Stoehr and G. E. Hill., "Intersexual differences in age-specific parental effort in the house finch.," *Etologia,* vol. 9, pp. 35-41, 2001.

[21] K. J. McGraw, W. Medina-Jerez and H. Adams., "Carotenoid-based plumage coloration and aggression during molt in male house finches.," *Behaviour,* vol. 144, pp. 165-178, 2007.

[22] L. Busin, N. Vandenbroucke and L. Macaire, ""Color spaces and image segmentation."," *Advances in imaging and electron physics,* vol. 151, pp. 65-168, 2008.

[23] R. W. Hunt, "Measuring Colour," in *Measuring Colour*, 3rd ed., England: Fountain Press, 1998, pp. 39-57.

[24] J. Schanda, Colorimetry, Wiley-Interscience., 2009.

[25] A. R. Smith, "Color gamut transform pairs," in *Proceedings of ACM SIGGRAPH*, vol. 12, pp. 12-19, 1978.

[26] A. Dempster, N. Laird and D. Rubin, "Maximum Likelihood from Incomplete Data via the EMAlgorithm," *Journal of the Royal Statistical,* vol. 39, no. 1, pp. 1-38, 1977.

[27] R. Duda, P. Hart and D. Stork, Pattern Classification, New York: John Wiley & Sons, 2001.

[28] A. C. Bovik, Handbook of image and video processing, Elsevier, 2010.

[29] A. Said and L. J.Karam, "Cell Migration Analysis using a Statistical Level-Set Segmentation on a Wavelet-Based Structure Tensor Feature Space," *7th IEEE International Symposium on Signal Processing and Information Technology (ISSPIT),* pp. 473-478, 2007.

[30] T. J. Bergman and J. C. Beehner, "A simple method for measuring colour in wild animals: validation and use on chest patch colour in geladas (Theropithecus gelada).," *Biological Journal of the Linnean Society,* vol. 94, no. 2, pp. 231-240, 2008.

[31] D. Kendal, C. E. Hauser, G. E. Garrard, S. Jellinek, K. M. Giljohann and a. et, "Quantifying Plant Colour and Colour Difference as Perceived by Humans Using Digital Images.," *PLoS ONE,* vol. 8(8): e72296., 2013.

[32] Adobe Photoshop. [Online] Available: http://www.photoshop.com/products

[33] GIMP 2.8. [Online] Available: http://www.gimp.org/

[34] ImageJ [Online] Available: http://rsb.info.nih.gov/ij/

[35] R. Montgomerie, "Analyzing colors," in *Hill GE, McGraw KJ, Eds. Bird Coloration: Mechanisms and Measurements*, vol. 1, Cambridge: Harvard University Press, 2006, pp. 90-147.

[36] Y. Vortman, "Measuring animal coloration in nature: A protocol for scoring colors based on the RGB model and Adigital photography software tool". [Online] Available: http://ibis.tau.ac.il/twiki/bin/view/Zoology/Lotem/YoniVortman

[37] D. Comaniciu and P. Meer, "Robust analysis of feature spaces: Color image segmentation," in *IEEE CVPR*, pp. 750-755, 1997.

[38] R. Szeliski, "Segmentation," in *Computer Vision:Algorithms and Applications*, New York, NY,, Springer-Verlag New York, Inc., 2010, pp. 289-296.

[39] P. Heckbert, "Color image quantization for frame buffer display," *ACM SIGGRAPH Computer Graphics,* vol. 16, no. 3, pp. 297-307, July 1982.

[40] D. Arthur and S. Vassilvitskii, "k-means++: The advantages of careful seeding," in *Proceedings of the eighteenth annual ACM-SIAM Symposium on Discrete Algorithms*, pp. 1027-1035, 2007.

[41] W. Y. Ma, Y. Deng and B. S. Manjunath, "Tools for texture/color based search of images," in *Proc. SPIE Human Vision and Electronic Imaging II*,vol. 3016, pp. 496-507, 1997.

[42] A. Mojsilovic, J. Kovacevic, J. Hu, R. J. Safranek and S. K. Ganapathy, "Matching and retrieval based on the vocabulary and grammar of color patterns," *IEEE Transactions of Image Processing,* vol. 1, no. 1, pp. 38–54, Jan. 2000.

[43] Y. Deng, B. S. Manjunath, C. Kenney, M. S. Moore and H. Shin, "An efficient color representation for image retrieval," *IEEE Transactions of Image Processing,* vol. 10, no. 1, pp. 140–147, Jan. 2001.

[44] A. Mojsilovic, J. Hu and E. Soljanin, "Extraction of perceptually important colors and similarity measurement for image matching, retrieval, and analysis," *IEEE Transactions of Image Processing,* vol. 11, no. 11, pp. 1238–1248, Nov. 2002.

[45] Y. Linde, A. Buzo and R. M. Gray, "An algorithm for vector quantizer design," *IEEE Transactions on Communications,* vol. 28, no. 1, pp. 84–95, Jan. 1980..

[46] J. Smith and S. F. Chang, "Single color extraction and image query," in *IEEE Int. Conf. Image Processing,*, vol. 3, pp. 528-531, 1995.

[47] J.-C. Terrillon, M. David and S. Akamatsu, "Automatic detection of human faces in natural scene images by use of a skin color model and of invariant moments," in *Proc. of the Third International Conference on Automatic Face and Gesture Recognition*, pp. 112-117, 1998.

[48] J. Yang, W. Lu and A. Waibel, "Skin-Color Modeling and Adaptation.," in *Proceedings of the Third Asian Conference on Computer Vision*, vol. II, pp. 687-694, 1998.

[49] J.-C. Terrillon, M. N. Shirazi, H. Fukamachi and S. Akamatsu, "Comparative performance of different skin chrominance models and chrominance spaces for the automatic detection of human faces in color images," in *Fourth IEEE International Conference on Automatic Face and Gesture Recognition*, pp. 54-61, 2000.

[50] T. S. Jebara and A. Pentland, "Parameterized structure from motion for 3D adaptive feedback tracking of faces," in *IEEE CVPR*, pp. 144-150, 1997.

[51] S. J. McKenna, S. Gong and Y. Raja, "Modeling facial color and identity with Gaussian mixtures," *Pattern Recognition,* vol. 31, no. 12, pp. 1883-1892, 1998.

[52] H. Akaike, "A new look at the statistical model identification," *IEEE Transactions on Automatic Control,* vol. 19, no. 6, pp. 716–723, 1974.

[53] Lemke-Rust, Kerstin and a. C. Paar, "Gaussian mixture models for higher-order side channel analysis," in *Cryptographic Hardware and Embedded Systems*, Berlin Heidelberg, pp. 14-27, 2007.

[54] J. Canny, "A computational approach to edge detection," *IEEE Transactions on Pattern Analysis and Machine Intelligence,* vol. 8, no. 6, pp. 679-698, 1986.

[55] R. R. Sokal and F. J. Rohlf, Biometry: the principles and practice of statistics in biological research, New York: W. H. Freeman and Co, 1981.

[56] C. M. Lessells and P. T. Boag, "Unrepeatable Repeatabilities: A Common Mistake," *The Auk,* vol. 104, no. 1, pp. 116-121, 1987.

APPENDIX A

ANOVA TABLES AND VARIANCE COMPONENT TABLES

Table A1. Inter-photo repeatability ANOVA table for measured hue in Dataset 1.

Source of variation	Degrees of freedom	Sum of squares	Mean squares	F ratio
Among groups for software	32	3517.907	109.935	807.676
Within groups for software	33	4.4917	0.13611	
Total variation for software	65	3522.398	54.1907	
Among groups for user 1	32	3400.399	109.69	203.451
Within groups for user 1	33	17.2527	0.5391	
Total variation for user 1	65	3417.652	54.2484	
Among groups for user 2	33	3574.499	108.318	137.959
Within group for user 2	32	26.695	0.7851	
Total variation for user 2	65	3601.194	53.749	
Among groups for user 3	33	3079.166	96.2239	34.5172
Within group for user 3	32	91.994	2.78771	
Total variation for user 3	65	3171.16	48.7871	

Table A2. Inter-photo repeatability variance components for measured hue in Dataset 1.

Component	Component variance	% of Total
Among groups for software	54.8992	99.8
Within groups for software	0.1361	0.2473
Total variance for software	55.0353	100
Among groups for user 1	54.5755	99.02
Within groups for user 1	0.5391	0.9782
Total variance for user 1	55.1147	100
Among groups for user 2	53.7665	98.6
Within groups for user 2	0.7851	1.4
Total variance for user 2	54.5516	100
Among groups for user 3	46.7181	94.4
Within groups for user 3	2.7877	5.6
Total variance for user 3	49.5058	100

Table A3. Inter-photo repeatability ANOVA table for measured saturation in Dataset 1.

Source of variation	Degrees of freedom	Sum of squares	Mean squares	F ratio
Among groups for software	32	1147.982	35.8744	373.633
Within groups for software	33	3.1685	0.0960	
Total variation for software	65	1151.151	17.71	
Among groups for user 1	32	2345.693	75.6675	18.4060
Within groups for user 1	33	131.5525	4.1110	
Total variation for user 1	65	2477.246	39.3214	
Among groups for user 2	32	2318.172	70.2476	18.7744
Within groups for user 2	33	127.216	3.7416	
Total variation for user 2	65	2445.389	36.4983	
Among groups for user 3	32	2820.612	88.1441	6.8004
Within groups for user 3	33	427.755	12.9623	
Total variation for user 3	65	3248.368	49.9749	

Table A4. Inter-photo repeatability variance components of measured saturation in Dataset 1.

Component	Component variance	% of Total
Among groups for software	17.8892	99.5
Within groups for software	0.0960	0.5339
Total variance for software	17.9852	100
Among groups for user 1	35.7782	89.7
Within groups for user 1	4.1110	10.3
Total variance for user 1	39.8892	100
Among groups for user 2	33.2529	89.9
Within groups for user 2	3.7416	10.1
Total variance for user 2	36.9946	100
Among groups for user 3	37.5909	74.4
Within groups for user 3	12.9622	25.6
Total variance for user 3	50.5532	100

Table A5. Inter-photo repeatability ANOVA table for measured value of Dataset 1.

Source of variation	Degrees of freedom	Sum of squares	Mean squares	F ratio
Among groups for software	32	2563.382	80.1057	1103.70
Within groups for software	33	2.3951	0.0725	
Total variation for software	65	2565.77	39.4735	
Among groups for user 1	32	4012.874	129.448	59.5332
Within groups for user 1	33	69.5800	2.1743	
Total variation for user 1	65	4082.454	64.8009	
Among groups for user 2	32	3789.824	114.843	73.3448
Within group for user 2	33	53.237	1.565	
Total variation for user 2	65	3842.061	57.359	
Among groups for user 3	32	4462.188	139.443	31.1564
Within group for user 3	33	147.6947	4.4756	
Total variation for user 3	65	4609.883	70.9213	

Table A6. Inter-photo repeatability variance components for measured value in Dataset 1.

Component	Component variance	% of Total
Among groups for software	40.0165	99.8
Within groups for software	0.0725	0.181
Total variance for software	40.0891	100
Among groups for user 1	67.4838	96.7
Within groups for user 1	4.4755	3.3
Total variance for user 1	71.9594	100
Among groups for user 2	56.6386	97.3
Within groups for user 2	1.5657	2.7
Total variance for user 2	58.2044	100
Among groups for user 3	63.6365	93.8
Within groups for user 3	2.1743	6.2
Total variance for user 3	65.8109	100

Table A7. Inter-photo repeatability ANOVA table for measured patch size in Dataset 1.

Source of variation	Degrees of freedom	Sum of squares	Mean squares	F ratio
Among groups for software	32	1.22e+11	3.82e+9	168.347
Within groups for software	33	7.496e+8	2.27e+7	
Total variation for software	65	1.23e+11	1.89e+9	
Among groups for user 1	32	1.47e+11	4.76e+9	8.42087
Within groups for user 1	33	1.81e+11	5.65e+8	
Total variation for user 1	65	1.66e+11	2.63e+9	
Among groups for user 2	32	7.26e+11	2.2e+10	14.0992
Within group for user 2	33	5.3e+10	1.56e+9	
Total variation for user 2	65	7.79e+11	1.2e+10	
Among groups for user 3	32	3.49e+11	1.1e+10	2.3250
Within group for user 3	33	1.55e+11	4.69e+9	
Total variation for user 3	65	5.04e+11	7.76e+9	

Table A8. Inter-photo repeatability variance components for measured patch size in Dataset 1.

Component	Component variance	% of Total
Among groups for software	1.90e+9	98.8
Within groups for software	2.27e+9	1.2
Total variance for software	1.92e+9	100
Among groups for user 1	3.10e+9	78.8
Within groups for user 1	4.69e+9	21.2
Total variance for user 1	7.80e+9	100
Among groups for user 2	1.02e+10	86.8
Within groups for user 2	1.55e+9	13.2
Total variance for user 2	1.17e+10	100
Among groups for user 3	2.09e+9	39.9
Within groups for user 3	5.64e+8	60.1
Total variance for user 3	2.66e+9	100

Table A9. Inter-photo repeatability ANOVA table for the measured hue in Dataset 2.

Source of variation	Degrees of freedom	Sum of squares	Mean squares	F ratio
Among groups for software	24	2889.127	120.38	12479.3
Within groups for software	25	0.2411	0.00965	
Total variation for software	49	2889.368	58.9667	
Among groups for user 1	24	3155.518	131.48	114.562
Within groups for user 1	25	28.6918	1.1476	
Total variation for user 1	49	3184.21	64.9839	
Among groups for user 2	24	3263.93	135.997	111.935
Within groups for user 2	25	30.3741	1.2149	
Total variation for user 2	49	3294.313	67.2309	
Among groups for user 3	24	3203.294	133.471	101.698
Within group for user 3	25	32.8104	1.3124	
Total variation for user 3	49	3236.104	66.0429	

Table A10. Inter-photo repeatability variance components for measured hue in Dataset 2.

Component	Component variance	% of Total
Among groups for software	60.1853	99.98
Within groups for software	0.0096	0.02
Total variance for software	60.1949	100
Among groups for user 1	65.1661	98.3
Within groups for user 1	1.1476	1.7
Total variance for user 1	66.3137	100
Among groups for user 2	67.3912	98.2
Within groups for user 2	1.2149	1.8
Total variance for user 2	68.6062	100
Among groups for user 3	66.0790	98.1
Within groups for user 3	1.3124	1.9
Total variance for user 3	67.3914	100

Table A11. Inter-photo repeatability ANOVA table for measured saturation in Dataset 2.

Source of variation	Degrees of freedom	Sum of squares	Mean squares	F ratio
Among groups for software	24	617.085	25.7119	1042.93
Within groups for software	25	0.6163	0.02465	
Total variation for software	49	617.70	12.6062	
Among groups for user 1	24	1228.33	51.1804	13.6175
Within groups for user 1	25	93.9608	3.7584	
Total variation for user 1	49	1322.291	26.9855	
Among groups for user 2	24	1434.365	59.7652	15.7884
Within groups for user 2	25	94.6345	3.7853	
Total variation for user 2	49	1528.99	31.2041	
Among groups for user 3	24	1214.123	50.5884	11.6292
Within group for user 3	25	108.7534	4.3501	
Total variation for user 3	49	1322.876	26.9975	

Table A12. Inter-photo repeatability variance components for measured saturation in Dataset 2.

Component	Component variance	% of Total
Among groups for software	12.8436	99.8
Within groups for software	0.0246	0.2
Total variance for software	12.8682	100
Among groups for user 1	23.7109	86.3
Within groups for user 1	3.7584	13.7
Total variance for user 1	27.4694	100
Among groups for user 2	27.9899	88.1
Within groups for user 2	3.7853	11.9
Total variance for user 2	31.7752	100
Among groups for user 3	23.1191	84.2
Within groups for user 3	4.3501	15.8
Total variance for user 3	27.4692	100

Table A13. Inter-photo repeatability ANOVA table for measured value in Dataset 2.

Source of variation	Degrees of freedom	Sum of squares	Mean squares	F ratio
Among groups for software	24	1509.457	62.8941	87790
Within groups for software	25	0.0179	0.0007	
Total variation for software	49	1509.475	30.8056	
Among groups for user 1	24	2291.522	95.4801	87.6520
Within groups for user 1	25	27.2327	1.0893	
Total variation for user 1	49	2318.755	47.3215	
Among groups for user 2	24	2364.833	98.5347	159.941
Within group for user 2	25	15.401	0.6160	
Total variation for user 2	49	2380.234	48.5762	
Among groups for user 3	24	2250.799	93.7833	72.4267
Within group for user 3	25	32.3718	1.2948	
Total variation for user 3	49	2283.17	46.5953	

Table A14. Inter-photo repeatability variance components for measured value in Dataset 2.

Component	Component variance	% of Total
Among groups for software	31.4466	100
Within groups for software	0.0007	0.0023
Total variance for software	31.4473	100
Among groups for user 1	47.1953	97.7
Within groups for user 1	1.0893	2.3
Total variance for user 1	48.2846	100
Among groups for user 2	48.9593	98.8
Within groups for user 2	0.6160	1.2
Total variance for user 2	49.5753	100
Among groups for user 3	46.2442	97.3
Within groups for user 3	1.2948	2.7
Total variance for user 3	47.5390	100

Table A15. Inter-photo repeatability ANOVA table for measured patch size in Dataset 2.

Source of variation	Degrees of freedom	Sum of squares	Mean squares	F ratio
Among groups for software	24	5.41e+11	2.3e+10	1075.22
Within groups for software	25	5.241e+8	2.1e+7	
Total variation for software	49	5.41e+11	1.1e+10	
Among groups for user 1	24	4.04e+11	1.7e+10	5.7628
Within groups for user 1	25	7.31e+10	2.92e+9	
Total variation for user 1	49	4.77e+11	9.74e+9	
Among groups for user 2	24	8.31e+11	3.5e+10	14.8202
Within group for user 2	25	5.84e+10	2.34e+9	
Total variation for user 2	49	8.9e+11	1.8e+10	
Among groups for user 3	24	3.92e+11	1.6e+10	3.7172
Within group for user 3	25	1.1e+11	4.4e+9	
Total variation for user 3	49	5.02e+11	1e+10	

Table A16. Inter-photo repeatability variance components for measured patch size in Dataset 2.

Component	Component variance	% of Total
Among groups for software	1.126e+10	99.8
Within groups for software	2.09e+7	0.2
Total variance for software	1.12e+10	100
Among groups for user 1	6.96e+9	70.4
Within groups for user 1	2.93e+9	29.6
Total variance for user 1	9.88e+9	100
Among groups for user 2	1.61e+10	87.4
Within groups for user 2	2.33e+9	12.6
Total variance for user 2	1.84e+10	100
Among groups for user 3	5.97e+9	57.6
Within groups for user 3	4.39e+9	42.4
Total variance for user 3	1.03e+10	100